nature communications

Article

https://doi.org/10.1038/s41467-025-61847-2

Microbiota-derived corisin accelerates kidney fibrosis by promoting cellular aging

Received: 13 January 2025

Accepted: 2 July 2025

Published online: 25 August 2025

Check for updates

Taro Yasuma[1,2,3,18], Hajime Fujimoto[4,18], Corina N. D'Alessandro-Gabazza[1,2,5,18], Masaaki Toda[1,18], Mei Uemura[3], Kota Nishihama[1,3], Atsuro Takeshita[1,3], Valeria Fridman D'Alessandro[1,2], Tomohito Okano[4], Yuko Okano[3], Atsushi Tomaru[4], Tomoko Anoh[1,4], Chisa Inoue[3], Manal A. B. Alhawsawi[5,6], Ahmed M. Abdel-Hamid[5], Kyle Leistikow[7], Michael R. King[7], Ryoichi Ono[8], Tetsuya Nosaka[8], Hidetoshi Yamazaki[9], Christopher J. Fields[10], Roderick I. Mackie[5,6,11], Xuenan Mi[12], Diwakar Shukla[12], Justine Arrington[13], Yutaka Yano[3], Osamu Hataji[14], Tetsu Kobayashi[2,4] ✉, Isaac Cann[5,6,11,15,16,17] ✉ & Esteban C. Gabazza[1,2,4,5,11] ✉

The increasing global prevalence of diabetic nephropathy poses substantial health and economic burdens. Currently, effective anti-fibrotic therapies for managing kidney fibrosis associated with chronic kidney disease are lacking. This study reveals corisin, a microbiota-derived peptide, as a central driver in the progression of diabetic kidney fibrosis. Corisin levels were found to be markedly elevated in the serum of diabetic chronic kidney disease patients relative to healthy controls, with strong correlations to advanced disease stages and declining renal function. In a murine model of kidney fibrosis, corisin levels were similarly heightened, directly contributing to increased inflammation and worsening fibrosis and renal impairment. Notably, the use of a monoclonal anti-corisin antibody significantly reduced nephropathy severity in diabetic mice. Through molecular dynamics simulations and experimental validation, we demonstrated that corisin interacts with human serum albumin, potentially enhancing its renal accumulation and pathological impact. The pathogenic mechanism of corisin involves the acceleration of cellular senescence and the induction of epithelial-mesenchymal transition and apoptosis in kidney cells. These findings underscore the critical role of corisin in progressive diabetic nephropathy and suggest a promising new target for therapeutic intervention.

The rising prevalence of diabetes mellitus (DM) has emerged as a critical global health challenge, imposing a substantial economic burden on societies worldwide[1–3]. Recent epidemiological data underscore the alarming magnitude of this issue, revealing that 536.6 million individuals, constituting an estimated prevalence of 10.5%, were affected by DM worldwide in 2021[4]. The prevalence is expected to rise to 12.2%, affecting 783.2 million individuals, by 2045[4]. The seriousness of the situation is compounded by the association of DM with elevated morbidity and mortality rates. According to the World Health Organization (WHO), there was a 3% increase in mortality rates due to DM across different age groups between 2000 and 2019, resulting in approximately 1.5 million deaths globally in 2019 directly attributed to DM[3]. The primary culprits contributing to the high morbidity and mortality rates associated with DM are microangiopathy and

A full list of affiliations appears at the end of the paper. ✉e-mail: ktetsu@clin.medic.mie-u.ac.jp; icann@illinois.edu; gabazza@med.mie-u.ac.jp

macroangiopathy[5–10]. Notably, diabetic nephropathy stands out as one of the most prevalent complications, assuming the role of the leading cause of chronic kidney disease and end-stage kidney disease[6,9,11,12]. This expanding diabetic population and the associated complications, particularly diabetic nephropathy, underscore the pressing need for comprehensive strategies to manage and mitigate the impact of diabetes on global health.

The unique functional and histopathological features of diabetic nephropathy include proteinuria, enhanced cell proliferation, elevated matrix deposition in the mesangium and renal interstitium, tubular atrophy, and thickening of the glomerular basement membrane, resulting in glomerulosclerosis and tubulointerstitial fibrosis, collectively contributing to a reduced glomerular filtration rate[13,14]. These fibrotic changes in the kidneys can lead to irreversible damage, ultimately culminating in end-stage kidney disease. Currently, there is no definitive cure for DM-associated kidney fibrosis. Treatment options primarily revolve around controlling hyperglycemia, proteinuria, and arterial hypertension, decreasing cardiovascular risk, alleviating symptoms, and implementing renal replacement therapies in cases of severely impaired kidney function. The primary effects of dysglycemia on the kidneys include injury, activation, and/or apoptosis of glomerular endothelial cells, podocytes, and tubular epithelial cells, as well as overactivation of the intrarenal renin-angiotensin-aldosterone system[13,15]. Recent studies suggest that alterations in the microbiome or dysbiosis may play a role in the progression of diabetic nephropathy[16–18]. Dysbiosis has been linked to excessive production and accumulation of bacterial metabolites, including urease, p-cresol, and acetate, potentially contributing to oxidative stress, kidney cell apoptosis, inflammation, and profibrotic activity[19–22]. Notably, recent studies demonstrated the presence of gut-derived bacteria within the kidneys of spontaneously hypertensive rats, and patients with arterial hypertension[23]. Dysbiosis has also been implicated in the sudden exacerbation of renal failure or acute kidney injury[24–26]. Additionally, our recent research identified corisin, a microbiota-derived peptide, as a potential contributor to podocyte and renal tubular cell apoptosis, further implicating the microbiome in the pathogenesis of kidney fibrosis[27,28].

Building upon this foundation, we hypothesized that corisin contributes to the progression of kidney fibrosis, a key pathological feature of diabetic CKD. Overall, our study demonstrates that elevated circulating corisin levels correlate with disease severity and renal dysfunction in DM patients and with increased kidney fibrosis in murine models. Systemic administration of corisin was associated with kidney fibrosis, while its inhibition attenuates the progression of diabetic nephropathy in experimental animal models. Mechanistically, corisin interacts with human serum albumin, facilitating its transport to the kidneys, where it accelerates cellular senescence and induces apoptosis or epithelial-mesenchymal transition, promoting fibrogenesis. These findings underscore the potential of targeting the corisin pathway as a promising strategy to mitigate the progression of diabetic nephropathy.

Results

High circulating levels of corisin in patients with diabetic CKD

We initially posited that the circulating concentration of microbiota-derived corisin is dysregulated in patients with diabetic CKD. To test this hypothesis, we quantified corisin levels in serum from this patient population (Supplementary Table 1). Our analysis revealed a marked elevation in serum corisin levels in patients with diabetic CKD compared to healthy controls. Furthermore, serum corisin levels were also significantly higher in patients with non-diabetic CKD relative to healthy individuals. However, no significant difference was observed between the diabetic and non-diabetic CKD groups. Notably, serum corisin concentrations were significantly elevated in diabetic CKD patients at stages G2 to G4 compared to those at stage G1 (Fig. 1A, B). Analysis of 24-hour urine collections demonstrated no significant differences between the G1 and G2-G4 subgroups in either the daily urinary excretion of corisin or albumin (Supplementary Fig. 1).

An inverse correlation was observed between serum corisin levels and estimated glomerular filtration rates (eGFR), while a direct correlation was noted with systolic blood pressure and serum creatinine and total cholesterol levels (Supplementary Fig. 2). We also conducted univariate and multivariate analyses, using eGFR as the dependent variable. Variables with a p-value of less than 0.05 in their univariate relationship with eGFR were included in the multivariate analysis. Serum corisin levels were independently and inversely correlated with eGFR, consistent with reduced renal clearance (Supplementary Table 2). In addition, baseline serum corisin levels exhibited an increasing trend in patients with diabetic nephropathy who experienced a greater decline in eGFR over a two-year follow-up period (>4 mL/min/1.73 m^2) compared to those with a lesser decline (<4 mL/min/1.73 m^2), suggesting a potential role of corisin in the progression of kidney function deterioration in diabetic CKD patients (Supplementary Fig. 3).

Staphylococcus species are the primary source of corisin in diabetic patients with CKD

We have previously isolated corisin and corisin-like peptides from the lung tissue of mice with lung fibrosis, identifying commensal or pathogenic bacteria from the *Staphylococcus* species as their main source[27,29]. After confirming the presence of corisin peptides in urine through immune assays, we aimed to determine the source of these peptides in patients with diabetic CKD. We prepared DNA from the urine of these patients and amplified DNA fragments encoding corisin/corisin-like peptides. To develop PCR primers that specifically amplify the DNA encoding the proapoptotic peptides in each urine sample, we created a large alignment of the polypeptide sequences of the IsaA-like transglycosylases from diverse bacteria. We identified two highly conserved sequences flanking the proapoptotic peptides (SVKAQF and WGTGSV), which facilitated the design of two primers, Corisin-F (5'ATCAGTTAAAGCTCAATTC) and Corisin-R (5'GCTACTGAACCAGTACCCCATG). This primer pair successfully amplified ~150 bp DNA fragments, the predicted size of the coding sequences for the proapoptotic peptides. Subsequent DNA sequencing and bioinformatics analysis of the corisin/corisin-like peptides in the urine samples revealed that they match those present in diverse *Staphylococcus* species with genomes reported in the Genbank database (Fig. 1C, D, Supplementary Dataset 1). These results confirm the presence of corisin and corisin-like peptides in human fluids and establish *Staphylococcus* species as their primary source in diabetic CKD patients.

High circulating and urine levels of corisin in mice with diabetic CKD

As kidney fibrosis is a hallmark of CKD, we sought to validate the abnormal corisin levels observed in patients with diabetic CKD by comparing plasma and urinary corisin levels between normal wild-type (WT) mice and kidney-specific transforming growth factor-β1 (TGFβ1) transgenic (TG) mice with kidney fibrosis. Plasma and urinary corisin levels were significantly elevated in TGFβ1 TG mice with kidney fibrosis compared to WT controls. In addition, plasma and urinary levels of TGFβ1 were significantly elevated in TGFβ1 transgenic (TG) mice compared to WT controls (Supplementary Fig. 4A–C). However, no significant correlations were observed between corisin and TGFβ1 levels in either plasma ($r = -0.09$, $p = 0.65$) or urine (−0.18, $p = 0.37$), suggesting that TGFβ1 may not directly regulate corisin expression.

To determine whether DM further exacerbates the abnormal levels of corisin, we measured and compared the levels of corisin in plasma and urine samples collected from diabetic and non-diabetic TGFβ1 TG mice with kidney fibrosis. We observed a significant increase in both plasma and urine levels of corisin in diabetic TGFβ1 TG mice with kidney fibrosis compared to their non-diabetic counterparts

https://doi.org/10.1038/s41467-025-61847-2

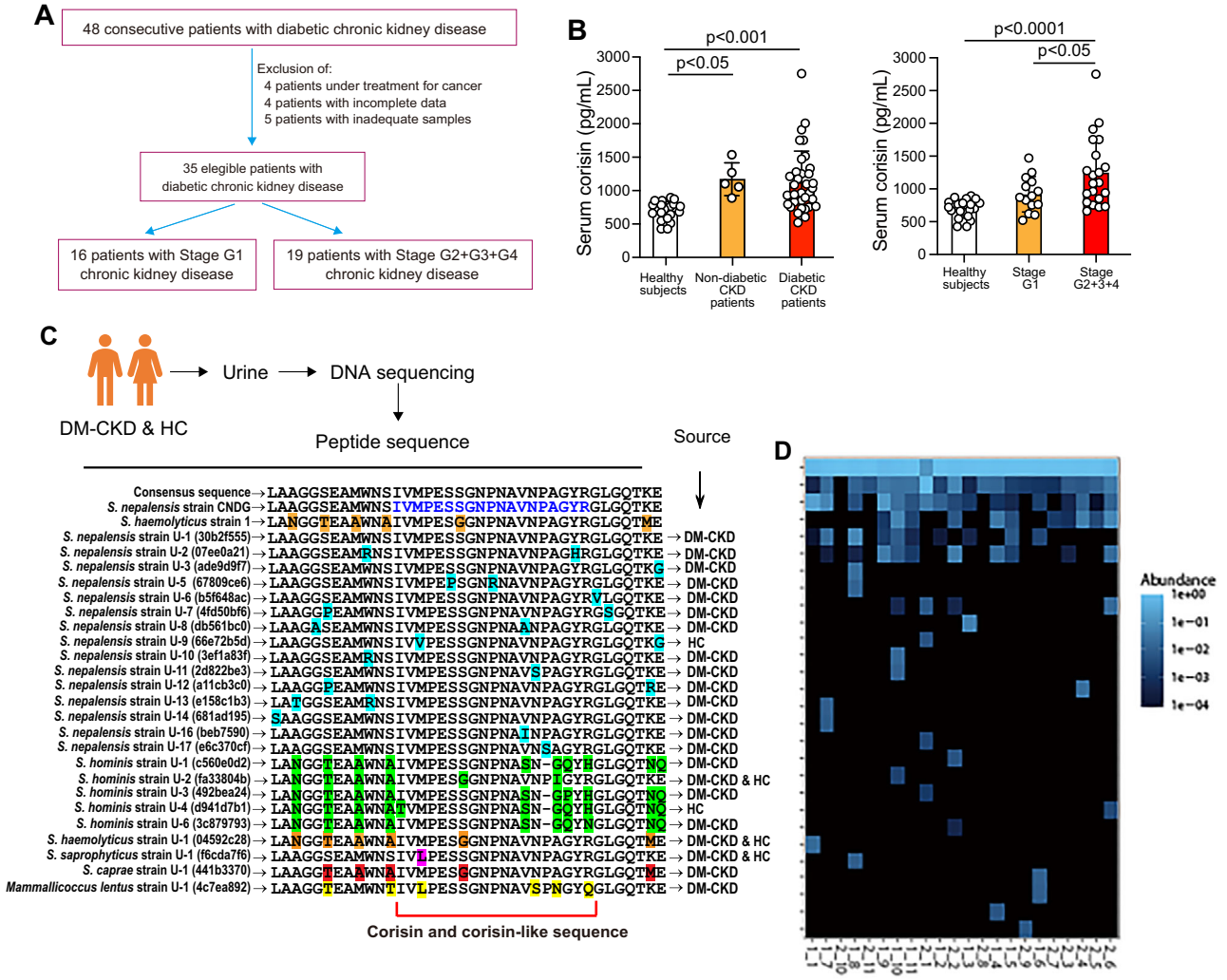

Fig. 1 | Increased serum levels of corisin in diabetic chronic kidney disease patients. A Thirty-five patients were enrolled in the study. Thirteen patients were excluded due to ongoing anticancer therapy, incomplete datasets, or suboptimal sample quality. **B** Data from 20 healthy subjects served as controls. Diabetic chronic kidney disease patients were allocated into two groups: one with stage G1 ($n = 16$) and another with stages G2, G3, and G4 ($n = 19$). Five patients with non-diabetic chronic kidney disease were also included in the study. Data are expressed as mean ± SD. Statistical significance was determined using one-way ANOVA followed by the Newman–Keuls *post hoc* test for comparisons among three groups. **C** Human corisin and corisin-like peptide sequences identified in the urine of patients with diabetic chronic kidney disease (DM-CKD) and healthy controls (HC). *Staphylococcus* species are the primary source of corisin in diabetic patients with chronic kidney disease. Sequences were aligned using DECIPHER, including two reference sequences (*S. nepalensis*: GenBank CP120099.1; *S. haemolyticus*: GenBank CP071512.1). Sequence IDs represent the closest species-level match, accompanied by a unique identifier corresponding to the original sequence. **D** A heatmap displaying read counts from sequence IDs, representing unique peptide sequences from the original amplicons, was used to normalize relative abundance across patients. The data are plotted on a $\log^{10}$ scale using phyloseq. The source data are available in the Source Data file.

(Supplementary Fig. 4D–F). To investigate whether similar alterations in circulating corisin levels occur in a different experimental model of DM, unilaterally nephrectomized WT mice, with or without diabetic nephropathy, were prepared, and plasma corisin levels were measured. In this model, unilateral nephrectomy accelerates the progression of diabetic nephropathy. Consistent with findings from TGFβ1 transgenic mice with spontaneous kidney fibrosis and TGFβ1 TG mice with diabetic nephropathy, plasma corisin levels were significantly elevated in WT mice with diabetic kidney fibrosis compared to non-diabetic WT controls (Supplementary Fig. 4G–I). Overall, these observations suggest a potential association between corisin and kidney fibrosis, particularly in diabetic conditions.

Systemic administration of corisin is linked to increased kidney fibrosis

Given our observations of elevated corisin levels in nephropathy-related conditions and the documented role of corisin in organ fibrosis exacerbation, we posited that corisin might contribute to nephropathy by accelerating the progression of kidney fibrosis[27,30]. To explore this hypothesis, we systemically administered synthetic corisin to TGFβ1 transgenic mice with kidney fibrosis, a model we have previously characterized[31]. Synthetic corisin or control scrambled peptide was administered intraperitoneally to the TGFβ1 TG mice thrice weekly for two weeks (Fig. 2A). The results revealed that TGFβ1 TG mice treated with corisin exhibited a significant increase in urinary levels of corisin, albumin, and albumin-to-creatinine ratio. The plasma levels of blood urea nitrogen (BUN) and the urinary levels of liver-type fatty acid-binding protein (L-FABP) were also significantly elevated in TGFβ1 TG mice receiving intraperitoneal corisin compared to their untreated counterparts (Fig. 2B, C). As expected, plasma corisin levels were significantly elevated in TGFβ1 TG mice receiving intraperitoneal synthetic corisin compared to their counterparts receiving the scrambled peptide. Quantitatively, the mean circulating corisin levels in corisin-treated mice were 2.2-fold higher than those observed in diabetic CKD

https://doi.org/10.1038/s41467-025-61847-2

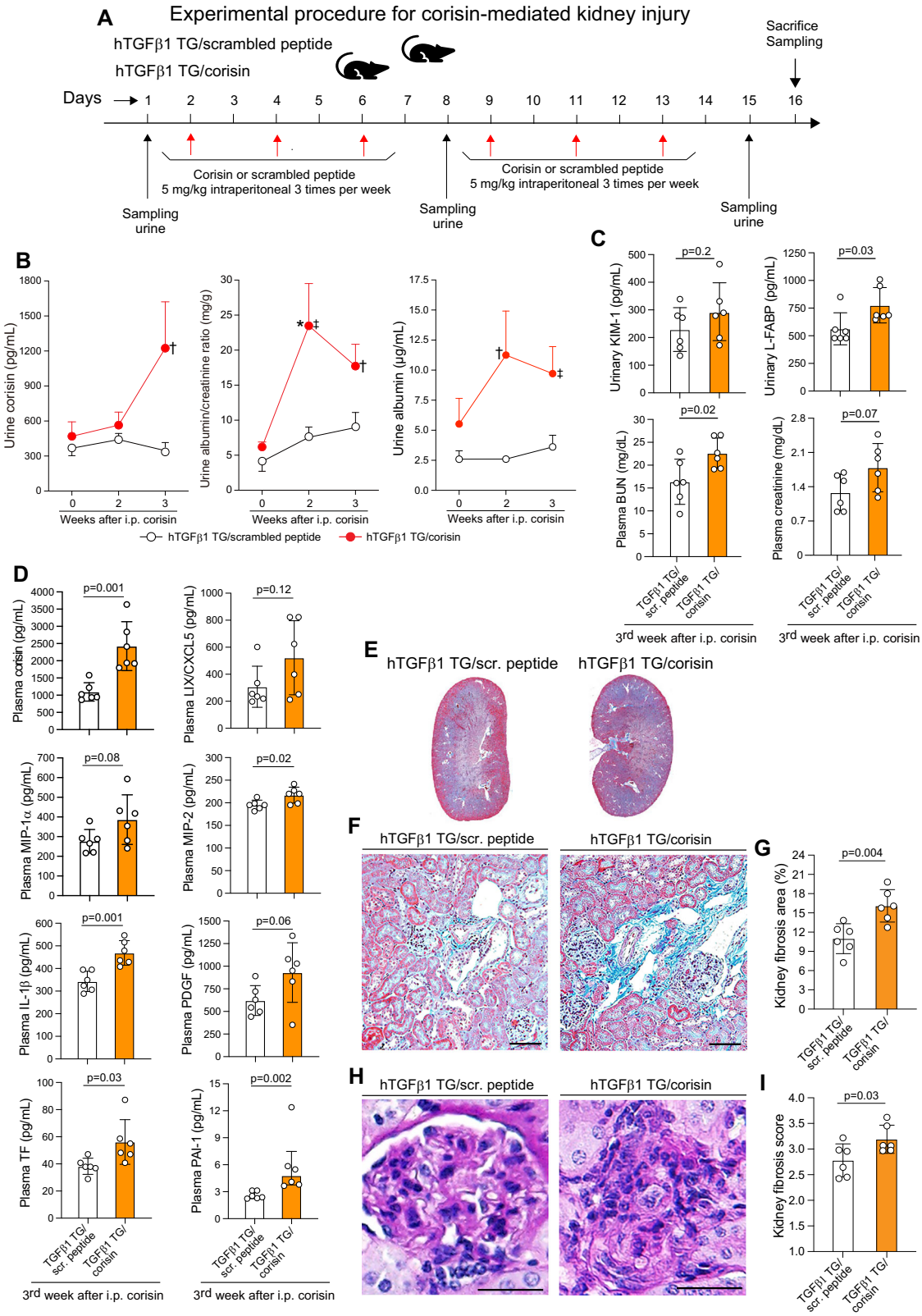

patients and 1.6-fold higher than those in diabetic TGFβ1 transgenic mice. The circulating levels of lipopolysaccharide-induced CXC chemokine (LIX/CXCL5), macrophage inflammatory protein-2 (MIP-2), interleukin-1β (IL-1β), platelet-derived growth factor (PDGF), tissue factor (TF), and plasminogen activator inhibitor-1 (PAI-1) were also increased in the corisin-treated mice compared to those receiving the scrambled peptide (Fig. 2D). Furthermore, renal dysfunction was associated with significantly increased fibrotic changes in the corisin-treated mice compared to those receiving the scrambled peptide (Fig. 2E–I). These findings suggest that corisin may contribute to the progression of chronic nephropathy by promoting inflammation and fibrosis in the kidney.

Fig. 2 | The administration of corisin induces acute kidney injury and exacerbation of kidney fibrosis in TGFβ1 transgenic mice with pre-existing renal injury. A Experimental plan for inducing acute kidney injury in TGFβ1 transgenic (TG) mice with pre-existing renal dysfunction. One group of transforming growth factor β1 (TGFβ1) TG mice (TGFβ1 TG/corisin; $n = 6$) received 5 mg/kg of body weight of synthetic corisin by intraperitoneal injection every two days for two weeks, and another group (TGFβ1 TG/scr. peptide; $n = 6$) received a similar dose of scrambled peptide following the same schedule and route of administration. **B** Urinary corisin, albumin, and creatinine were measured as described under materials and methods. Number of mice: TGFβ1 TG/corisin, $n = 6$; TGFβ1 TG/scr. peptide, $n = 6$. Data are presented as mean ± SEM. Statistical significance was assessed using ANOVA with the Newman-Keuls test for longitudinal data and an unpaired one-sided t-test for comparisons between two groups. $^{*}p < 0.05$ vs week 0; $\dagger p = 0.02$ and $\ddagger p = 0.01$ vs TGFβ1 TG/scrambled peptide group. **C** The urinary levels of kidney injury molecule-1 (KIM-1), liver-type fatty acid-binding protein (L-FABP), blood urea nitrogen (BUN), and creatinine were measured as described under material and methods. Number of mice: TGFβ1 TG/corisin, $n = 6$; TGFβ1 TG/scr. peptide, $n = 6$. Data are presented as mean ± SD. Statistical significance was determined using a two-sided unpaired t-test. **D** Plasma levels of lipopolysaccharide-induced CXC chemokine (LIX/CXCL5), macrophage inflammatory protein-2 (MIP-2), interleukin-1β (IL-1β), platelet-derived growth factor (PDGF), tissue factor (TF), and plasminogen activator inhibitor-1 (PAI-1) were measured using enzyme immunoassays. Normally distributed data are presented as mean ± SD, while skewed data are expressed as the median with interquartile range. Number of mice: TGFβ1 TG/corisin, $n = 6$; TGFβ1 TG/scr. peptide, $n = 6$. Statistical significance was assessed using a two-sided unpaired t-test for normally distributed data and the two-sided Mann-Whitney U test for skewed data. **E**–**I** Masson's trichrome and periodic acid–Schiff staining of renal tissues from both groups of mice. Renal fibrosis was quantified using WinROOF imaging software. Scale bars indicate 100 μm in (**D**) and 50 μm in (**F**). Number of mice: TGFβ1 TG/corisin, $n = 6$; TGFβ1 TG/scr. peptide, $n = 6$. Data are presented as mean ± SD. Statistical significance was determined using a two-sided unpaired t-test. The source data are available in the Source Data file.

Corisin inhibition mitigates the progression of nephropathy under diabetic conditions

Considering the potential involvement of corisin in the progression of kidney fibrosis and the well-established association of DM as a risk factor for progressive nephropathy and end-stage kidney disease, we hypothesized that inhibiting corisin may alleviate kidney fibrosis under diabetic conditions[32]. To test this hypothesis, we evaluated whether administering a neutralizing anticorisin monoclonal antibody (mAb) could mitigate the progression of nephropathy in TGFβ1 TG mice with DM. Through streptozotocin injection, DM was induced in TGFβ1 TG mice with pre-existing renal dysfunction (Fig. 3A). The diagnosis of DM in the mouse models was confirmed by blood glucose levels and intraperitoneal glucose tolerance test results (Fig. 3B). Upon confirmation of DM, one group of mice received the anticorisin mAb, while another group received an IgG control, administered intraperitoneally three times a week for eight weeks. The mice were sacrificed at the end of the ninth week after streptozotocin administration. Throughout the treatment period, urine and plasma samples were collected sequentially from each experimental group. It is noteworthy that, in a preliminary experiment, the degree of kidney fibrosis was compared between DM TG mice treated with intraperitoneal injections of control IgG and saline, revealing no significant difference and thereby supporting the use of control IgG as an appropriate negative control in this experiment (Supplementary Fig. 5).

By the 12th week of the study, TG mice treated with the anticorisin neutralizing mAb exhibited a significant reduction in plasma creatinine and blood urea nitrogen (BUN) levels, along with a decreased urinary albumin-to-creatinine ratio. Urinary levels of L-type fatty acid-binding protein, a marker of tubular cell injury, were also significantly improved compared to control mice (Fig. 3B). Treatment with the anti-corisin neutralizing mAb markedly reduced extracellular matrix deposition, as well as circulating levels of chemokines (LIX/CXCL5), growth factors (total TGFβ1, active TGFβ1, PDGF, CTGF), and collagen I (Fig. 3C–H). Furthermore, diabetic mice treated with the anti-corisin mAb showed significantly decreased renal deposition of corisin (Supplementary Fig. 6A, B; Supplementary Fig. 7A, B; Supplementary Fig. 8A, B), accompanied by reduced apoptosis in both glomerular and tubular epithelial cells (Supplementary Fig. 9A, B). Consistent with previous reports identifying macrophages as mediators of tissue injury, fibrosis, and functional decline in diabetic chronic kidney disease (CKD)[33,34], we observed increased macrophage infiltration in diabetic mice with kidney fibrosis, which was significantly attenuated in mice treated with the anti-corisin mAb (Supplementary Fig. 9C, D). Overall, these findings suggest that corisin contributes to renal tissue injury, inflammation, and functional impairment associated with kidney fibrosis under diabetic conditions.

Enrichment of corisin-expressing *Staphylococcus* in fecal samples from diabetic TGF-β1 transgenic mice and elevated circulating levels of I-FABP2, a marker of intestinal epithelial injury, in patients with diabetic CKD

Having established the increased circulating levels of corisin and its role in kidney fibrosis, we next investigated whether its potential source resides within the gut microbiome. To this end, we employed the previously described PCR primers, which selectively amplify a ~150 bp DNA fragment encoding proapoptotic peptides, to analyze fecal samples from WT mice and TGFβ1 TG mice with STZ-induced DM and kidney fibrosis. Our analysis revealed significant enrichment in *Staphylococcus* species expressing corisin in fecal samples from diabetic TGFβ1 TG mice compared to control mice (Supplementary Fig. 10A, B). Gut microbiota dysbiosis can increase intestinal permeability, promoting the translocation of microbial products into the systemic circulation[35]. To evaluate intestinal epithelial injury, we measured circulating levels of intestinal fatty acid-binding protein 2 (I-FABP2) and found them to be significantly elevated in diabetic patients with CKD compared to non-diabetic CKD and healthy controls (Supplementary Fig. 10C). These findings collectively suggest that under diabetic conditions, increased intestinal permeability and microbial dysbiosis enhance the systemic release of corisin, indicating that enhanced production contributes to elevated circulating levels.

Molecular dynamic simulation predicts corisin interaction with human serum albumin

Following the demonstration that corisin may be implicated in the development of diabetic nephropathy, we explored how microbiome-derived corisin targets the kidneys. Serum albumin is known for its role as a carrier for various endogenous substances, including those from the microbiome, such as short-chain fatty acids and indole derivatives[36]. We hypothesized that corisin interacts with serum albumin to reach the kidneys and contribute to nephropathy pathogenesis. To interrogate this hypothesis, we conducted molecular dynamics simulations to analyze the interactions between corisin and human serum albumin and bovine serum albumin. Human serum albumin is composed of a single polypeptide chain containing 585 amino acid residues, organized into three α-helical domains labeled I, II, and III[36–38]. The amino acid sequence of human albumin exhibits a high degree of homology with bovine albumin, sharing 77.5% identity[39]. We employed AlphaFold-Multimer[40] to model the configurations of corisin bound to human serum albumin (HSA) and bovine serum albumin (BSA). The predictive analysis suggests that corisin interacts with domains I and III of HSA, whereas it predominantly associates with domain II of BSA (Fig. 4A, B). A 100 ns molecular dynamics simulation was conducted on both HSA-corisin and BSA-corisin complexes using OpenMM[41]. Subsequently, the interaction energies of these complexes were quantified

https://doi.org/10.1038/s41467-025-61847-2

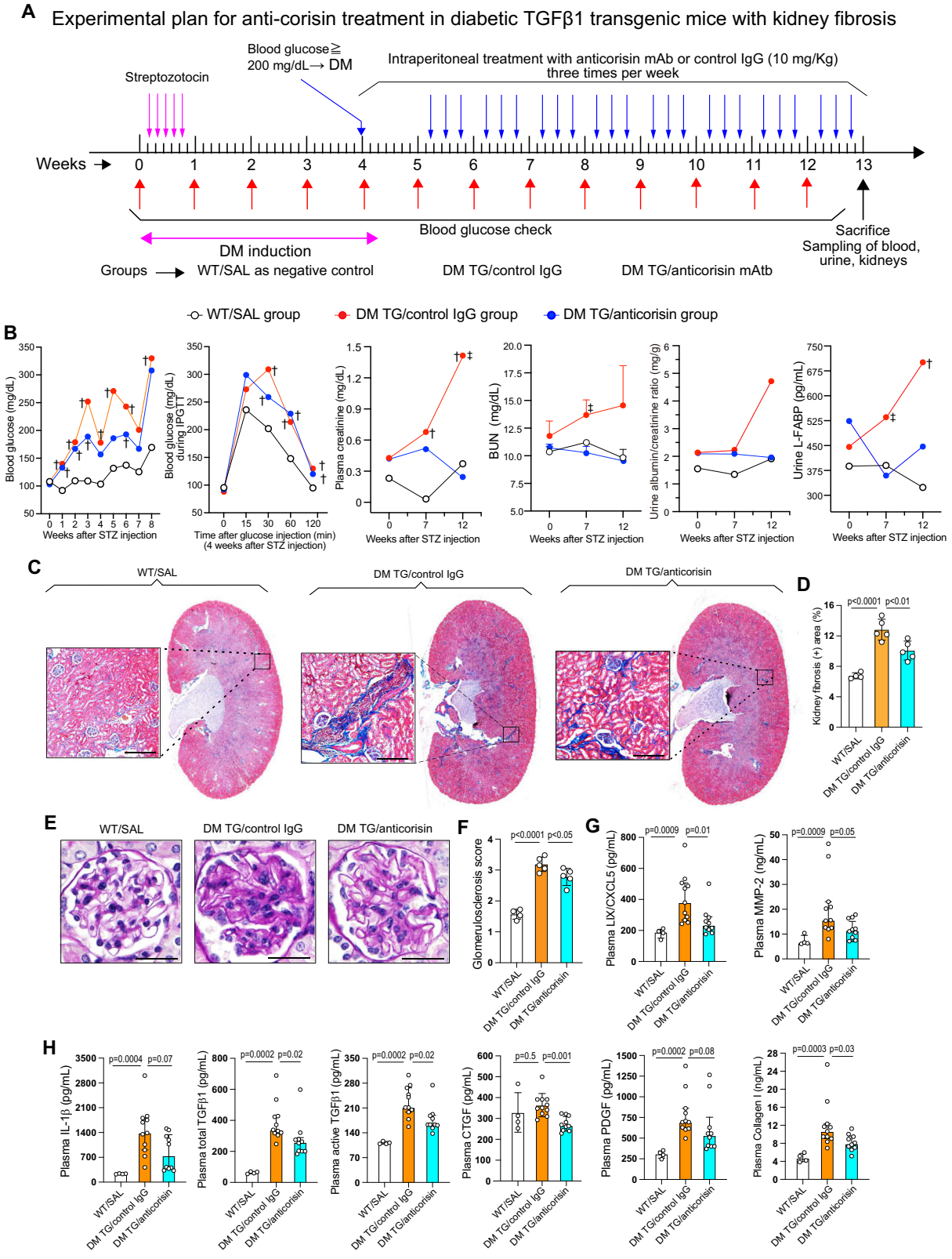

using the Linear Interaction Energy (LIE) method in CPPTRAJ[42]. The results reveal lower interaction energy for the HSA-corisin complex, with a significant difference of approximately -22.3353 kcal/mol. These findings suggest that corisin may form a stable complex with human serum albumin, indicating that, like other microbiome-derived metabolites, albumin could serve as a carrier for corisin to reach distant organs, including the kidneys.

Experimental validation of corisin-human serum albumin interaction

We conducted Western blotting to validate the computational analysis suggesting the interaction of corisin with human serum albumin. Various concentrations of synthetic corisin or its scrambled peptide were incubated with a defined concentration of recombinant human serum albumin (rhAlb) at room temperature for 10 min. The mixtures

Fig. 3 | Treatment with the anticorisin antibody inhibits the progression of kidney fibrosis under diabetic conditions. A Experimental plan. Diabetic TGFβ1 TG mice were divided into the following groups. One group (DM TG/anticorisin) received 10 mg/kg of body weight of anticorisin mAb by intraperitoneal injection three times a week for eight weeks, while another group (DM TG/control IgG) received a similar dose of IgG control. Following the same sampling schedule, a wild-type (WT) ($n = 4$) group was also included. **B** Blood glucose levels throughout the experiment, intraperitoneal glucose tolerance test (IPGTT), plasma creatinine, blood urea nitrogen (BUN), urine albumin/creatinine ratio, and urinary liver-type fatty acid-binding protein (L-FABP) levels. $n = 5$ for DM TG/control IgG and DM TG/anti-corisin; $n = 4$ for WT/SAL. Normally distributed data are presented as the mean, while skewed data are presented as the median. Statistical significance was assessed using ANOVA followed by either the Newman-Keuls or Dunn's post hoc test, as appropriate; all tests were two-sided. †$p < 0.05$ vs WT/SAL across the same week. **C, D** Paraffin-embedded kidney tissue samples for collagen staining with trichrome acid. $n = 5$ in DM TG/control IgG and DM TG/anticorisin groups, and $n = 4$ in the WT/SAL group. Renal fibrosis was quantified using WinROOF. Scale bars represent 500 μm. Data are presented as mean ± SD. Statistical significance was assessed using ANOVA and the Newman-Keuls test; all tests were two-sided. **E, F** Paraffin-embedded kidney tissue samples for Periodic acid-Schiff (PAS) staining. Scale bars represent 50 μm. $n = 5$ in DM TG/control IgG and DM TG/anticorisin groups, and $n = 4$ in the WT/SAL group. Data are presented as mean ± SD. Statistical significance was assessed using ANOVA and the Newman-Keuls test; all tests were two-sided. **G, H** The plasma levels of lipopolysaccharide-induced CXC chemokine/C-X-C motif chemokine 5 (LIX/CXCL5), interleukin-1β (IL-1β), matrix metalloproteinase-2 (MMP-2), platelet-derived growth factor (PDGF), total and active transforming growth factor β1 (TGFβ1), connective tissue growth factor (CTGF), and collagen I were measured by enzyme-linked immune assays. $n = 11$ in DM TG/control IgG, $n = 10$ in DM TG/anticorisin groups, and $n = 4$ in the WT/SAL group. Normally distributed data are presented as mean ± SD, while skewed data are expressed as the median with interquartile range. Statistical significance was assessed using ANOVA followed by the Newman-Keuls or Dunn's post hoc test, as appropriate; all tests were two-sided. The source data are available in the Source Data file.

were then subjected to electrophoresis and Western blotting using an anticorisin mAb. Samples containing corisin and rhAlb displayed multiple bands at approximately 35, 46, 50, and 69 kDa, with band intensity increasing proportionally with corisin concentration, indicating co-localization and interaction of corisin with human albumin (Fig. 4C). In contrast, no bands were observed in samples containing the scrambled peptide. Membrane stripping followed by treatment with an anti-human albumin antibody showed uniformly intense bands across all lanes (Fig. 4D).

To confirm the co-localization of synthetic corisin with recombinant human serum albumin during electrophoresis, we conducted mass spectrometry. A specific quantity of synthetic corisin was dissolved in either 0.5% rhAlb or physiological saline and incubated at room temperature for 10 min. The samples were then subjected to electrophoresis followed by Coomassie blue staining (Supplementary Fig. 11). The stained bands corresponding to 35 kDa were excised, and the sequences of the proteins and peptides were analyzed using mass spectrometry. We compared the proteins and peptides present in the gels loaded with human albumin, with or without corisin. The results, including the list of identified proteins and peptides, are presented in Supplementary Data Set 2. Mass spectrometry analysis revealed that corisin coexisted with human albumin in the gel loaded with both albumin and corisin, whereas corisin was absent in the gel loaded solely with albumin. These observations further support the co-localization and interaction of corisin with human albumin.

We conducted an immunoprecipitation assay to further corroborate the formation of a complex between corisin and human albumin. Recombinant human albumin and synthetic corisin were mixed and incubated at 37 °C for 30 min. Subsequently, anticorisin mAb was added to the reaction mixture and incubated at 4 °C for 30 min. Protein G agarose beads were then added to the mixture and incubated further. After thoroughly washing the protein G agarose beads, the precipitated proteins were eluted by adding sodium dodecyl sulfate loading buffer and centrifugation. The eluted proteins' supernatant was subjected to gel electrophoresis and stained with Coomassie blue. The results demonstrated the co-precipitation of corisin with human albumin (Fig. 4E, lane 6), providing additional evidence of the interaction and complex formation between corisin and human albumin.

We also demonstrated through Western blotting that the corisin peptide interacts with human and mouse serum albumin from a commercial source and with serum albumin from patients with diabetic nephropathy and healthy subjects (Fig. 4F, G), independently of pH conditions (Supplementary Fig. 12A, B). In addition, our findings indicate that the majority of corisin in serum exists in a bound form, with free corisin being nearly undetectable (Supplementary Fig. 13). Overall, the results of these validation experiments strongly support the molecular interaction between albumin and corisin, suggesting a potential role for albumin in facilitating the transport of corisin to peripheral organs. This observation could have significant implications for understanding the mechanisms by which microbiome-derived corisin influences distant tissues and contributes to disease pathogenesis.

Enhanced proapoptotic activity of corisin in a human albumin-enriched solution

Previous studies have demonstrated that the conformational structure, stability, and functional properties of peptides can be significantly enhanced through complex formation with albumin[43–48]. Based on these findings, and given our observation that corisin interacts with human albumin, we hypothesized that synthetic corisin is structurally unstable when isolated in solution. We further propose that its interaction with human albumin improves the structural conformation of corisin, thereby enhancing its stability and functional activity. To validate this hypothesis, we utilized molecular dynamics simulations to examine the folding patterns of synthetic corisin in solution, initiating from both the native folded and unfolded states. Employing Markov State Models, we captured the thermodynamics and kinetics of distinct folded states, with the resulting free energy landscape (Supplementary Fig. 14A) delineating the energy barriers between different conformational states of the peptide.

We focused on the sole α-helix present between Val2 and Ser6 in the native structure, using this inter-residue distance, approximately 3.2 Å in the native peptide, as a key metric to monitor the folding progress. Additionally, the fraction of native contacts was employed as another crucial metric. Together, both the inter-residue distance and the fraction of native contacts provided a comprehensive depiction of the peptide's folding-free energy landscape. We observed three minima in the landscape, each representing distinct conformational states (Supplementary Fig. 14B). In state 1, the peptide exhibits a high fraction of native contacts, about 0.78, with a Val2-Ser6 distance of approximately 3 Å. In state 2, while the sole α-helix remains stable, other peptide parts lose native contact. In state 3, the peptide loses the α-helix structure entirely. This observation also provides insights into kinetic transitions across these three states, indicating that reaching state 1, characterized by a high ratio of interactions resembling the native structure, requires a significantly longer time. These results support our hypothesis that synthetic corisin alone is impaired in adopting its native conformation in solution.

Further investigations included 150-nanosecond molecular dynamics simulations to assess if corisin undergoes conformational changes upon interacting with human serum albumin. The root-mean-square deviation (RMSD) of corisin from its native structure, exceeding

https://doi.org/10.1038/s41467-025-61847-2

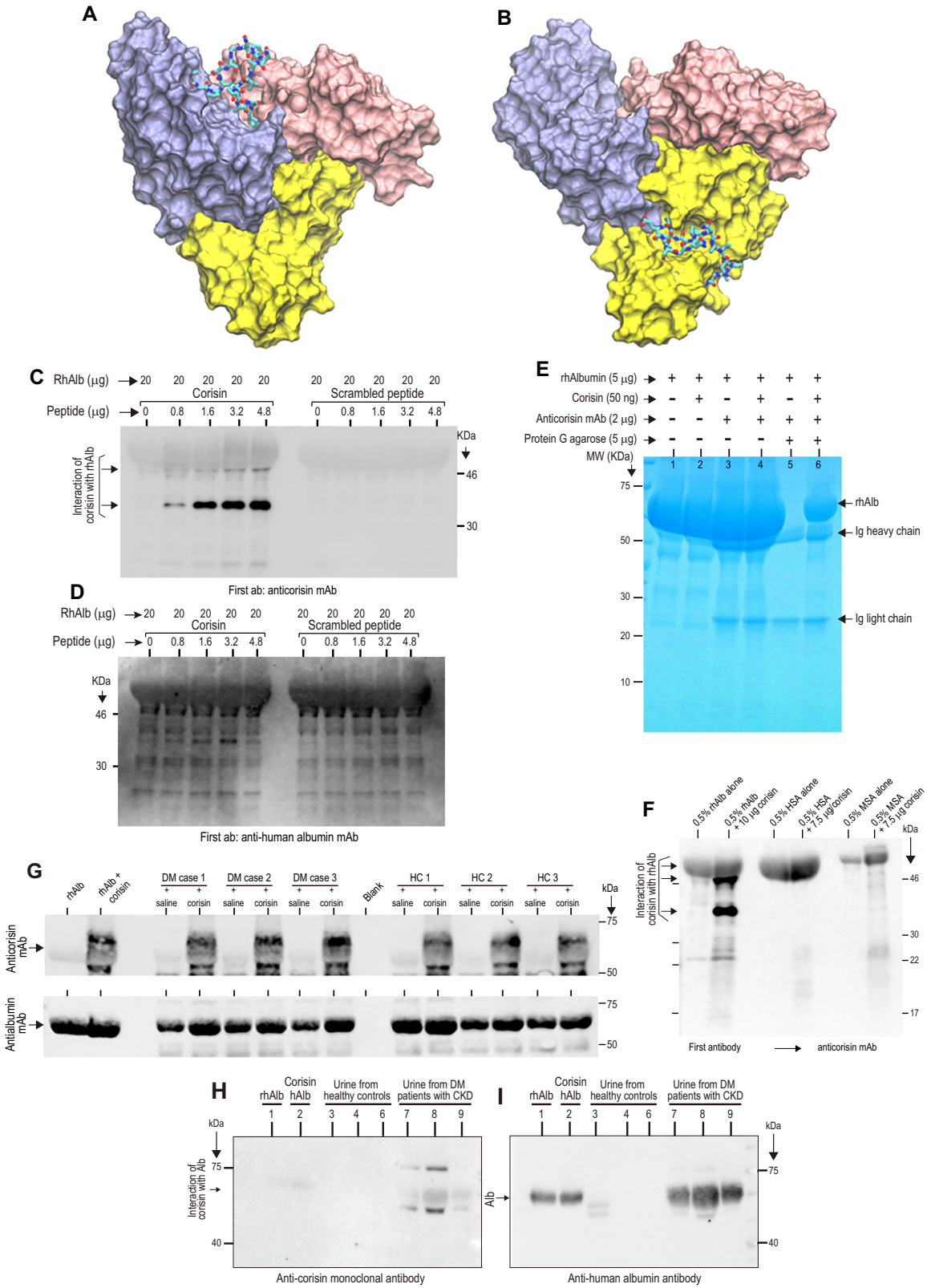

2 Ångstroms during this interaction, suggests significant conformational alterations (Supplementary Fig. 14C). Subsequent experiments tested whether this interaction enhances the proapoptotic efficacy of synthetic corisin. We cultured normal renal proximal tubule epithelial cells in varying concentrations of corisin diluted in 0.5% recombinant human serum albumin suspended in saline and compared them with cells cultured in equivalent concentrations of corisin in saline. The results showed that corisin diluted in 0.5% recombinant human albumin induced apoptosis in a dose-dependent manner, with a significantly higher percentage of apoptotic cells than those treated with saline alone (Supplementary Fig. 15A, B). Similar outcomes were observed in human Caki-2 tubular epithelial cells and normal human podocytes stimulated with corisin in the presence or absence of 0.5% recombinant human albumin. Comparative flow cytometry analysis revealed that

Fig. 4 | Corisin interacts with serum human albumin. A, B The predicted interaction structure of human serum albumin-corisin and bovine serum albumin-corisin by molecular dynamic simulations. Human serum albumin and bovine serum albumin are shown in surface representation, and domains I, II, and III are shown in pink, yellow, and ice blue, respectively. The corisin is shown in licorice representation. **C, D** Western blotting showing the interaction of corisin with recombinant human albumin (rhAlb) in vitro. A fixed concentration of rhAlb was combined with concentrations of synthetic corisin or scrambled peptide and incubated at room temperature for 10 min. The mixture underwent sodium dodecyl-sulfate polyacrylamide gel electrophoresis (SDS-PAGE), followed by Western blotting using anti-corisin monoclonal antibody (mAb) or anti-rhAlb antibody. The experiment was independently repeated three times with similar results. **E** Co-immunoprecipitation of corisin with rhAlb. Synthetic corisin was incubated with rhAlb, treated with an anti-corisin mAb, and immunoprecipitated using protein G agarose beads. rhAlb was not immunoprecipitated by the anti-corisin mAb and protein G agarose beads alone (lane 5). In the presence of corisin, rhAlb was successfully co-immunoprecipitated by the anti-corisin mAb and protein G agarose beads (lane 6). The experiment was independently repeated three times with similar results. Ig, immunoglobulin; MW, molecular weight. **F** Corisin interacts with human and mouse serum albumin. A predetermined concentration of human serum albumin (HSA) or mouse serum albumin (MSA) was incubated with synthetic corisin. The mixture was subjected to SDS-PAGE and Western blotting using an anti-corisin monoclonal antibody. The experiment was independently repeated three times with similar results. **G** Corisin interacts with human serum albumin derived from both patients with diabetic nephropathy and healthy individuals. Serum samples were diluted (1:20) and incubated for 10 min with corisin (4 μg) diluted in saline. As a control, a mixture containing corisin (4 μg) and rhAlb (5 μg) was prepared. Each mixture was then subjected to electrophoresis, followed by Western blot analysis using mAb specific for corisin or human albumin. The experiment was independently repeated three times with similar results. **H, I** Complex formation between corisin and albumin in the urine of diabetic CKD patients. Urine samples from 3 diabetic patients with chronic kidney disease (CKD) and 3 healthy subjects were concentrated 5 times, and 5 μL of each sample were subjected to SDS-PAGE, followed by Western blotting using an anti-corisin mAb (left panel) or anti-human albumin antibody (right panel). DM diabetes mellitus.

corisin in 0.5% recombinant human albumin significantly increases the percentage of apoptotic Caki-2 cells and podocytes compared to those treated with corisin in saline (Supplementary Fig. 15C–F). These findings suggest that the proapoptotic activity of corisin is significantly potentiated in the presence of human albumin, likely due to the interaction and complex formation between corisin and human albumin. Building on these observations, we subsequently employed corisin diluted in a human albumin solution for our in vitro studies.

In addition, the effect of corisin in 0.5% rhAlb on the expression of anti-apoptotic factors was assessed. Corisin in rhAlb significantly downregulated the expression of Bcl-2, Bcl-xL, apoptosis inhibitor 2 (cIAP2), and survivin in primary human renal tubular epithelial cells, an effect that was reversed by anti-corisin mAb co-treatment (Supplementary Fig 16A, B). Moreover, cell cycle analysis of both human primary podocytes and renal primary tubular epithelial cells demonstrated that corisin in 0.5% rhAlb, markedly increased the sub-G1 and G1 populations while decreasing the S-phase population (Supplementary Fig. 17A–D). These alterations were ameliorated by co-treatment with the anti-corisin monoclonal antibody. Consistent with these findings, both cell proliferation and proliferation rate were significantly reduced following corisin exposure (Supplementary Fig. 17E, F). These findings indicate that corisin impairs cell cycle progression and proliferation while promoting apoptosis in renal epithelial cells.

Complex formation between corisin and albumin in the urine of diabetic CKD patients

The demonstration that corisin interacts with human albumin and that this interaction enhances its cell injury capacity prompted the hypothesis that corisin forms complexes with albumin in the urine of patients exhibiting albuminuria. To test this hypothesis, urine samples from patients with diabetic CKD and from healthy controls were subjected to electrophoresis, followed by Western blot analysis using monoclonal antibodies against corisin and human albumin. Fragmentation and polymeric complexes of albumin have been reported in urine of DM patients[49,50]. Western blot results revealed bands exceeding 60 kDa and 40 kDa in all urine samples from patients with diabetic nephropathy but no bands in samples from healthy controls (Fig. 4H, I). These findings suggest that corisin is indeed complexed with albumin in the urine of patients with albuminuria, potentially mediating the adverse effects associated with albuminuria[51–53].

Corisin penetrates kidney cells via the albumin receptor cubilin to target the mitochondria

Previous studies have demonstrated that corisin specifically targets mitochondria[27,29]. After establishing that corisin interacts with human albumin, we investigated whether corisin penetrates kidney cells through albumin receptors to target the mitochondria. We focused on renal tubular epithelial cells and podocytes, as these cell types, unlike mesangial cells, express albumin receptors. Initially, we cultured Caki-2 tubular renal epithelial cells and primary human podocytes with fluorescein isothiocyanate (FITC)-labeled corisin or a FITC-labeled scrambled peptide dissolved in 0.5% human albumin. Following the addition of a Mito-tracker, we assessed changes in mitochondrial staining. Cells treated with FITC-labeled corisin exhibited dual staining of green and red, indicating mitochondrial targeting by corisin, unlike those treated with the scrambled peptide (Fig. 5A–D).

Subsequently, we pretreated human podocytes with small interfering RNA (siRNA) targeting several albumin receptors, including cubilin, megalin, CD36, SPARC (secreted protein acidic and rich in cysteine), and the neonatal Fc receptor (FcRn), which is encoded by the FCGRT gene. After exposure to FITC-labeled corisin dissolved in 0.5% human albumin, we observed significant inhibition of mRNA expression for all tested albumin receptors by their respective siRNAs. However, only the pretreatment with cubilin siRNA significantly suppressed the mitochondrial targeting by corisin (Fig. 5E–G). These results suggest that the albumin receptor cubilin mediates corisin's penetration into cells to specifically target the mitochondria.

Cellular entry of corisin in the absence of human albumin

To investigate whether corisin can penetrate cells independently of albumin, normal primary renal tubular epithelial cells were cultured in the presence of corisin-FITC diluted in either 0.5% recombinant human albumin (rhAlb) or saline. The intracellular uptake of corisin was tracked and quantified. The results demonstrated that corisin can partially penetrate cells even in the absence of albumin, suggesting the existence of alternative mechanisms for cellular entry (Supplementary Fig. 18A, B). These findings indicate that internalization of corisin may not be solely dependent on albumin binding and raise the possibility that alternative mechanisms, such as endocytosis, may contribute to its cellular uptake. Further investigation is warranted to elucidate the precise pathways involved.

Corisin induces senescence of parenchymal renal cells to accelerate kidney fibrosis

After elucidating how corisin targets renal tissues and penetrates kidney cells, we investigated the potential mechanism by which corisin could be involved in the progression of kidney fibrosis. Previous studies have shown that corisin exacerbates pulmonary fibrosis and acute lung injury by inducing mitochondria-mediated apoptosis in alveolar epithelial cells and promoting an inflammatory response[27,29,54]. Furthermore, the present study recapitulated the apoptotic activity of corisin on normal human podocytes and renal tubular epithelial cells (Supplementary Fig. 15A–F),

https://doi.org/10.1038/s41467-025-61847-2

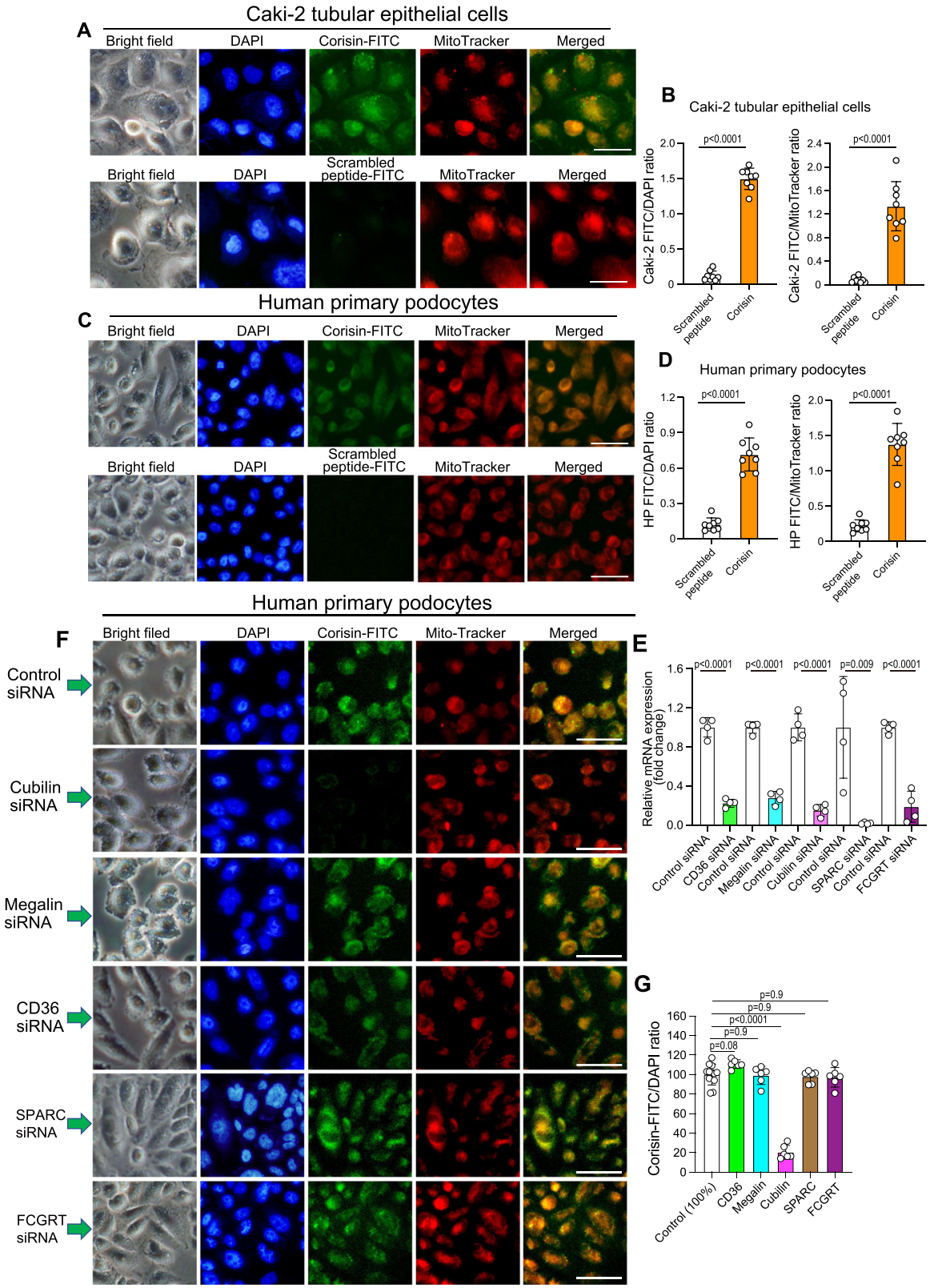

as previously reported[28]. Dysfunctional cell death disrupts the glomerular filtration barrier and tubular integrity, leading to proteinuria, reduced glomerular filtration rate (GFR), and tubular dysfunction[55,56]. Therefore, the apoptotic activity of corisin on renal parenchymal cells may also be a critical contributor to the pathogenesis of nephropathy.

Importantly, dysregulation of apoptosis is closely linked to senescence and the development of age-related diseases, including kidney fibrosis[57,58]. As organisms age, the accumulation of cellular damage and oxidative stress leads to increased apoptotic activity, contributing to tissue degeneration and functional decline[57,58]. Our previous research has demonstrated that corisin-induced apoptosis is associated with the activation of the intrinsic mitochondrial apoptotic pathway and the elevated production of reactive oxygen species[28,29]. Based on the foregoing observations, we hypothesized that corisin-associated apoptosis is

Fig. 5 | Corisin penetrates kidney cells via the human albumin receptor cubilin to target mitochondria. A–D, Human Caki-2 cell lines and normal human primary podocytes were cultured to near confluence, then treated with fluorescein isothiocyanate (FITC)-labeled corisin (corisin-FITC) or FITC-labeled scrambled peptide for 4 h. MitoTracker was added 30 min before fixation to label mitochondria, and cells were subsequently imaged via microscopy. The fluorescence intensities of F-actin and DAPI were quantified using ImageJ. Scale bars represent 20 μm. $n = 8$ replicates. Data are presented as mean ± SD. Statistical analysis was conducted using a two-sided unpaired t-test. **E–G**, Normal human primary podocytes were cultured for 48 h with siRNA targeting *CD36*, megalin, cubilin, *SPARC*, and *FCGRT*, and the relative expression of albumin receptors was evaluated. $n = 4$ replicates. Data are expressed as mean ± SD. Statistical comparison between each receptor-specific siRNA and its corresponding control siRNA was performed using a two-sided unpaired t-test. In a separate experiment, cells were cultured under the same conditions and then treated with corisin-FITC, MitoTracker, and DAPI and observed using fluorescence microscopy. The fluorescence intensities of F-actin and DAPI were quantified using ImageJ, an open-source software from the National Institutes of Health (NIH). Scale bars represent 20 μm. $n = 8$ replicates. $n = 12$ in control and $n = 6$ in remaining groups. Data are presented as mean ± SD. Statistical analysis was conducted using ANOVA followed by Dunnett's test; all tests were two-sided. The source data are available in the Source Data file.

part of the aging process induced by corisin during kidney fibrosis. To test this hypothesis, we treated primary human podocytes and human renal tubular epithelial cells with corisin and evaluated the activity of senescence-associated β-galactosidase (SAβGal), a marker of aging, and the mRNA expression of senescence markers, including tumor protein p53 (*TP53*, p53), Ki-67 (*MKI67*), and the cyclin-dependent kinase inhibitors *CDKN2B* (p15), *CDKN2A* (p16), *CDKN1A* (p21), and *CDKN1B* (p27)[59,60]. Additionally, we assessed components of the senescence-associated secretory phenotype (SASP), such as matrix metalloproteinase-12 (MMP-12) and osteopontin (SPP1)[59,60].

Corisin significantly enhanced the activity of SAβGal in human primary podocytes, human renal primary tubular epithelial cells, and the Caki-2 tubular epithelial cell line compared to controls. This enhanced activity was significantly reversed by culturing the cells in the presence of the anticorisin mAb21A (Fig. 6A–F). The expression of the senescence markers p16, p21, p27, p53, and SPP1 was significantly increased by corisin in both human podocytes and renal tubular epithelial cells compared to control cells. Conversely, Ki-67 expression was significantly decreased by corisin in both cell types. Compared to controls, the relative mRNA expression of MMP-12 was significantly increased by corisin treatment in podocytes but not in tubular epithelial cells (Fig. 6G, H). The effects of corisin on the mRNA expression of p21, p27, p53, and SPP1 were significantly blocked by treating the cells with anticorisin mAb. Similarly, the effect of corisin on the relative mRNA expression of Ki-67 was significantly inhibited in human renal tubular epithelial cells in the presence of anticorisin mAb (Fig. 6G, H). Abnormal nuclear morphology is a hallmark of senescent cells[61]. In line with this, human primary podocytes and renal primary tubular epithelial cells cultured in the presence of corisin exhibited an increased nuclear area, nuclear perimeter, and reduced circularity compared to controls. Notably, these nuclear abnormalities were significantly ameliorated by treatment with anti-corisin mAb (Supplementary Fig. 19A, B; Supplementary Fig. 20A, B). We also evaluated the expression of p21 (Fig. 6I, J), and p53 (Supplementary Fig. 21A, B) in diabetic TGFβ1 TG mice with kidney fibrosis by immunohistochemistry and found that corisin induced enhanced protein expression in diabetic mice with kidney fibrosis compared to counterpart mice treated with anticorisin mAb. Overall, these observations indicate that corisin-associated senescence induction in renal parenchymal cells may play an essential role in the progression of kidney fibrosis.

Enhanced expression of corisin and p21 in renal tissue from CKD patients

Previous research has demonstrated that p21 expression remains elevated in the renal tissue of CKD patients, even after improvements in blood glucose levels[62]. This persistent elevation is associated with the severity of diabetic kidney disease and serves as a marker of sustained renal damage[62]. In this study, we assessed the presence of corisin, apoptotic cells, and p21 expression in renal tissue from CKD patients using immunohistochemistry and compared it to normal renal tissue. Consistent with our observations in mouse models of diabetic TGFβ1 TG mice with kidney fibrosis, immunostaining for corisin, the senescence markers p21, and apoptotic cells were significantly increased in renal tissue from CKD patients compared to control tissue (Supplementary Fig. 22A, B). These findings further support the translational relevance of our mouse model results to human disease.

Corisin induces epithelial-mesenchymal transition in kidney parenchymal cells

Given the data above showing the potential involvement of corisin in senescence, the general knowledge that senescence and epithelial-mesenchymal transition (EMT) share common regulatory pathways in fibrosis, the role of EMT in facilitating the escape of cells from senescence, and the influence of the SASP on tissue remodeling and fibrosis, we hypothesized that corisin might also induce EMT in kidney parenchymal cells[63–65]. To test this hypothesis, we cultured human primary podocytes and human renal proximal tubule epithelial cells in the presence of corisin and evaluated markers of EMT. Podocytes and human renal proximal tubule epithelial cells cultured with corisin displayed a spindle-shaped morphology with significantly enhanced filamentous actin staining compared to control cells. Additionally, the intensity of filamentous actin was significantly reduced in cells treated with corisin plus the anticorisin mAb (Fig. 7A–D). The mRNA expression of α-smooth muscle actin (α-SMA), fibronectin, and collagen I was significantly increased by corisin in both podocytes and renal tubular epithelial cells compared to controls. Anti-corisin mAb significantly inhibited the increased expression of α-SMA and fibronectin in podocytes, as well as α-SMA, fibronectin, and collagen I in renal tubular epithelial cells. Furthermore, the mRNA expression of TGFβ1 was significantly elevated in podocytes treated with corisin, but this effect was significantly reduced by the anti-corisin mAb (Fig. 7E, F). These results suggest that corisin can directly promote fibrogenesis by inducing EMT in kidney parenchymal cells.

Single-cell RNA sequencing analysis reveals distinct transcriptional profiles in corisin-treated cells

Single-cell RNA sequencing analysis was performed to evaluate the transcriptional impact of corisin on human renal primary proximal tubular epithelial cells, comparing corisin-treated cells with those treated with a scrambled peptide control. The violin plots show significantly higher expression levels, while the Uniform Manifold Approximation and Projection (UMAP) plots confirm higher expression intensities across the cell population for various senescence-related and SASP markers, including cyclin-dependent kinase inhibitor 1 A (*CDKN1A*), serpin family E member 1 (*SERPINE1*), C-X-C motif chemokine ligand 8 (*CXCL8*), insulin-like growth factor binding protein 5 (*IGFBP5*), heparin-binding EGF-like growth factor (*HBEGF*), and EMT markers such as tropomyosin 2 (*TPM2*) and transgelin (*TAGLN*) (Fig. 8A, B). The expression of other EMT markers, including myosin light chain 9 (*MYL9*) and calponin 1 (*CNN1*), was also significantly upregulated in corisin-treated cells compared to scrambled peptide controls (Fig. 8C). Additionally, several other SASP markers were significantly elevated in the presence of corisin compared to the scrambled peptide, including growth arrest and DNA-damage-inducible alpha (*GADD45A*), myelocytomatosis oncogene (*MYC*), fibroblast growth factor 1 (*FGF1*), tumor necrosis factor (*TNF*), C-C motif

https://doi.org/10.1038/s41467-025-61847-2

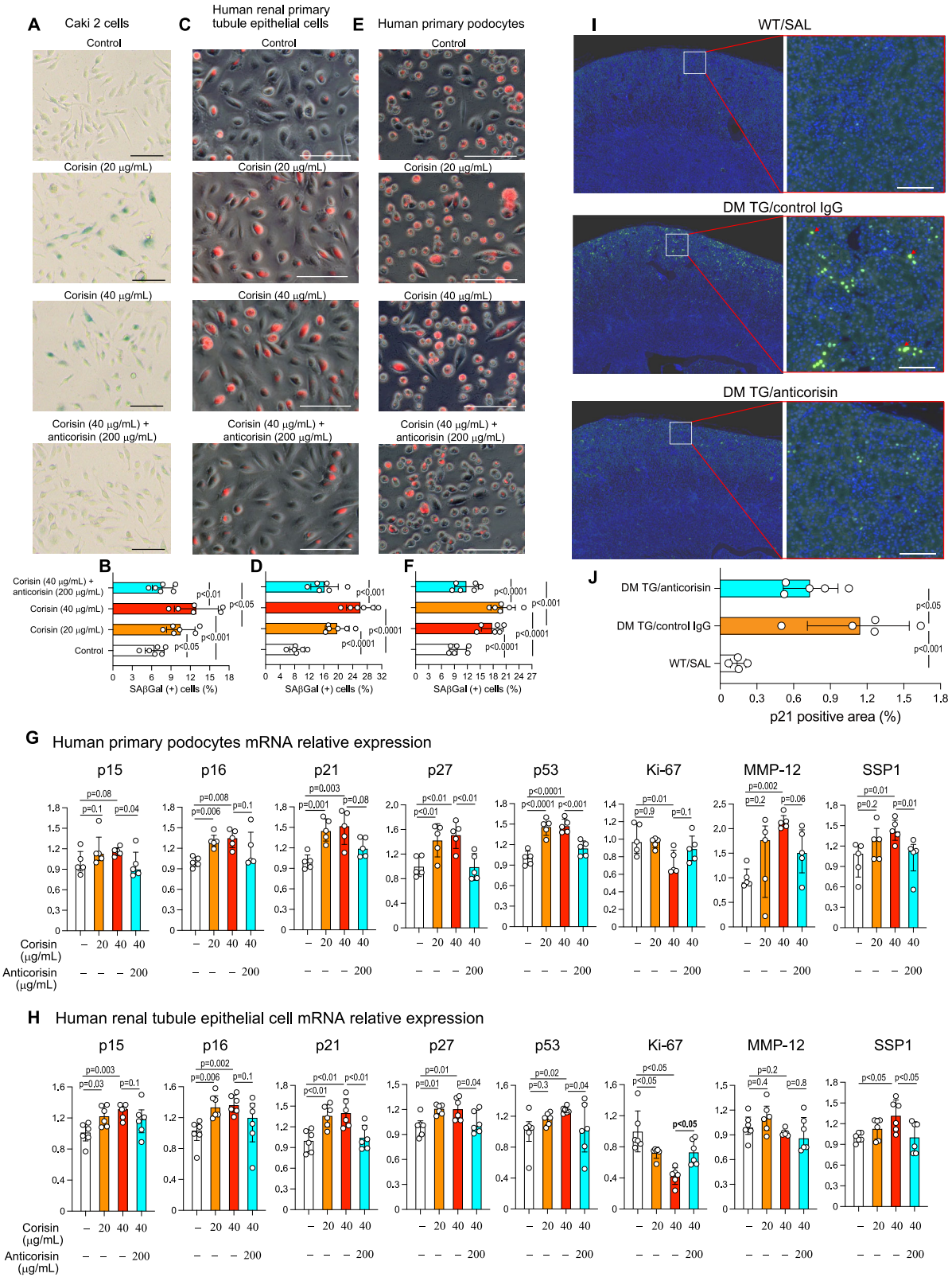

chemokine ligand 20 (*CCL20*), amphiregulin (*AREG*), inhibin subunit beta A (*INHBA*), C-X-C motif chemokine ligand 5 (*CXCL5*), C-X-C motif chemokine ligand 3 (*CXCL3*), and nerve growth factor (*NGF*) (Fig. 8D).

The relationship between cellular senescence and EMT after corisin stimulation was evaluated using single-cell analysis. Specifically, expression levels of mesenchymal markers, including α-smooth muscle actin (*ACTA2*), *CNN1*, *TAGLN*, and *TPM2*, were compared between cells with high and low expression of the senescence marker p21, using contingency table analysis. Chi-square testing indicated no significant increase in mesenchymal marker expression in cells with elevated p21 levels, suggesting that senescence does not directly drive EMT at the single-cell level during corisin stimulation (Supplementary Fig. 23A–D). Notably, *CXCL8* (IL-8) and growth differentiation factor 15 (*GDF15*), key components of the senescence-associated secretory

Fig. 6 | Corisin induces increased expression of senescence markers in kidney cells. A–F Induction of senescence-associated β-galactosidase (SAβGal) activity by corisin. Human Caki-2 cells (left panels), human primary renal tubular epithelial cells (middle panels), and normal human primary podocytes (right panels) were cultured in the absence or presence of 20 or 40 μg/mL of corisin, diluted in 0.5% recombinant human albumin (rhAlb), or 40 μg/mL of corisin with anti-corisin antibody. SAβGal activity was measured, and %SAβGal-positive cells was counted across multiple high-power fields using immunofluorescence microscopy. Scale bars represent 50 μm. Control, $n = 6$; corisin (20 μg/mL), $n = 6$; corisin (40 μg/mL), $n = 6$; corisin (40 μg/mL) + anticorisin (200 μg/mL), $n = 6$. Data are expressed as the mean ± SD. Statistical analysis by ANOVA followed by the Newman-Keuls test; all tests were two-sided. **G–H** Increased mRNA expression of senescence-associated factors in kidney cells by corisin. Normal human podocytes ($n = 6$) and normal human primary tubular epithelial cells ($n = 5$) were cultured in the absence or presence of 20 and 40 μg/mL corisin, diluted in 0.5% recombinant human albumin, or 40 μg/mL of corisin with anti-corisin antibody for 48 h. mRNA expression levels of cyclin-dependent kinase inhibitors p15 (*CDKN2*), p16 (*CDKN2A*), p21 (*CDKN1A*), p27 (*CDKN1B*), p53 (*TP53*), Ki-67 (*MKI67*), matrix metalloproteinase-12 (*MMP12*), and secreted phosphoprotein 1 (*SPP1*, also known as osteopontin) were evaluated by RT-PCR. Normally distributed data are presented as mean ± SD, while skewed data are expressed as the median with interquartile range. Statistical significance was assessed using ANOVA with the Newman-Keuls or Dunn's test; all tests were two-sided. **I, J** Anticorisin antibody inhibits the expression of senescence markers. Diabetes mellitus (DM) was induced in transforming growth factor β1 (TGFβ1) transgenic (TG) mice by streptozotocin. The mice were divided into a DM TG/control IgG group ($n = 5$) and a DM TG/anticorisin group ($n = 5$). Wild-type (WT) mice injected intraperitoneally with saline (SAL, $n = 4$) served as controls. Paraffin-embedded kidney tissue sections were prepared for p21 immunofluorescent staining. Green immunofluorescent signals (red arrows) indicate p21 expression. The p21-positive area was quantified using WinROOF. Scale bars represent 100 μm. Data are presented as mean ± SD. Statistical significance was evaluated by ANOVA followed by the Newman-Keuls test; all tests were two-sided. The source data are available in the Source Data file.

phenotype (SASP), were significantly upregulated in p21-high cells (Supplementary Fig. 24A, B). These findings imply that senescence and EMT are unlikely to co-occur within individual corisin-stimulated cells. Instead, EMT may result from SASP factors secreted during corisin-induced senescence rather than being a direct consequence of cellular senescence. Similarly, no significant increase in the proapoptotic markers p53, BAX and caspase 3 was observed in cells exhibiting elevated p21 levels, suggesting that senescence and apoptosis likely occur in distinct cell populations during corisin stimulation (Supplementary Fig. 25A–C).

A heatmap demonstrates the distinct transcriptional profiles of key upregulated and downregulated genes in corisin-treated cells compared to scrambled peptide controls (Fig. 9A). The volcano plot analysis highlights the most significantly upregulated genes in corisin-treated cells, including *CNN1*, *CXCL5*, *IGFBP5*, *INHBA*, p53-induced protein with a death domain 1 (*PIDD1*), and wingless-type MMTV integration site family, member 7 A (*WNT7A*), with fold changes exceeding 2 and P-values below 0.05. Conversely, genes such as coiled-coil domain containing 160 (*CCDC160*) and krüppel-like factor 15 (*KLF15*) were among those significantly downregulated (Fig. 9B).

Pathway enrichment analysis using Kyoto Encyclopedia of Genes and Genomes (KEGG) terms revealed significant enrichment of pathways associated with p53 signaling, cellular senescence, and interleukin-17 (IL-17) signaling, among others. Notably, pathways involved in cell cycle regulation, cytokine-cytokine receptor interaction, and cancer-related pathways were also highlighted, indicating a broad impact of corisin on processes linked to inflammation, senescence, and cell proliferation (Fig. 9C).

Categorization of the differentially expressed genes by their biological roles revealed increased expression of markers associated with the DNA damage response (blue cluster), cellular senescence (red cluster), myofibroblast-like factors (green cluster), and senescence-associated secretory phenotype (yellow cluster) in corisin-treated cells compared to scrambled peptide controls (Fig. 9D).

These results collectively suggest that corisin stimulation in renal tubular epithelial cells promotes pathways associated with the DNA damage response, induces cellular senescence, contributes to the development of a senescence-associated secretory phenotype, and enhances myofibroblast-like differentiation. This further indicates that corisin may play a significant role in driving renal fibrosis by promoting both cellular senescence and a fibrotic phenotype.

Discussion

This study demonstrates that increased corisin release by the microbiome in patients with diabetic CKD and mice with kidney fibrosis correlates with disease severity and renal dysfunction, contributes to the progression of kidney fibrosis, and interacts with human serum albumin to facilitate its transport to the kidneys, where it accelerates cellular senescence and induces epithelial-mesenchymal transition.

The involvement of microbial dysbiosis in the pathogenesis of kidney fibrosis in diabetic CKD has garnered increasing attention due to its significant impact on inflammation, metabolic disturbances, and overall kidney function. Disruption of the gut microbiota is associated with heightened systemic inflammation and altered immune responses, which are crucial in the progression of kidney fibrosis[66]. Dysbiosis has also been linked to the activation of the intrarenal renin-angiotensin system, further contributing to kidney injuries in diabetic nephropathy[67]. Additionally, microbial dysbiosis can participate in overproduction and accumulation of bacterial metabolites, including albumin-bound uremic toxins such as indoxyl sulfate, p-cresyl sulfate, phenyl sulfate, and 4-ethylphenyl sulfate[19–22]. These metabolites contribute to oxidative stress, kidney cell apoptosis, inflammation, and profibrotic activity, exacerbating kidney damage in diabetic nephropathy[68,69]. However, the potential of specific microbiome-derived metabolites as reliable biomarkers for dysbiosis or therapeutic targets remains uncertain[66,70]. Our previous research found elevated levels of corisin, a microbiome-derived peptide, in the blood of patients with various severe conditions, including idiopathic pulmonary fibrosis with acute exacerbation, COVID-19-associated acute lung injury, and acute cholangitis[27,30,71]. Corisin induces apoptosis of parenchymal cells, including those in the lungs and kidneys, and promotes inflammation by stimulating the secretion of inflammatory cytokines and chemokines and activating the coagulation system[28,29]. However, its role in diabetic nephropathy remained unclear. In this study, we recapitulated the apoptotic effects of corisin on kidney cells using primary human podocytes and renal tubular epithelial cells and demonstrated that an anti-corisin mAb significantly attenuates corisin-induced cellular damage in vitro while mitigating kidney fibrosis and dysfunction in diabetic mice. Furthermore, we observed that elevated circulating corisin levels in diabetic patients with CKD and in mice with diabetic kidney fibrosis correlate with renal dysfunction and fibrosis progression. Interestingly, serum corisin levels were also significantly elevated in non-diabetic patients with CKD compared to healthy controls, suggesting that dysregulation of corisin may also occur in CKD of non-diabetic etiology. These observations underscore the role of corisin in the progression of kidney fibrosis and highlight its potential as a therapeutic target in this debilitating condition. However, the extent of corisin's interaction with other uremic nephrotoxins that accumulate during diabetic nephropathy, as well as the magnitude of their additive effects, remains unclear and warrants further investigation.

Dysregulated apoptosis is intricately linked to cellular senescence. With aging, cells accrue damage and oxidative stress, heightening apoptotic activity that contributes to tissue degeneration and fibrosis,

https://doi.org/10.1038/s41467-025-61847-2

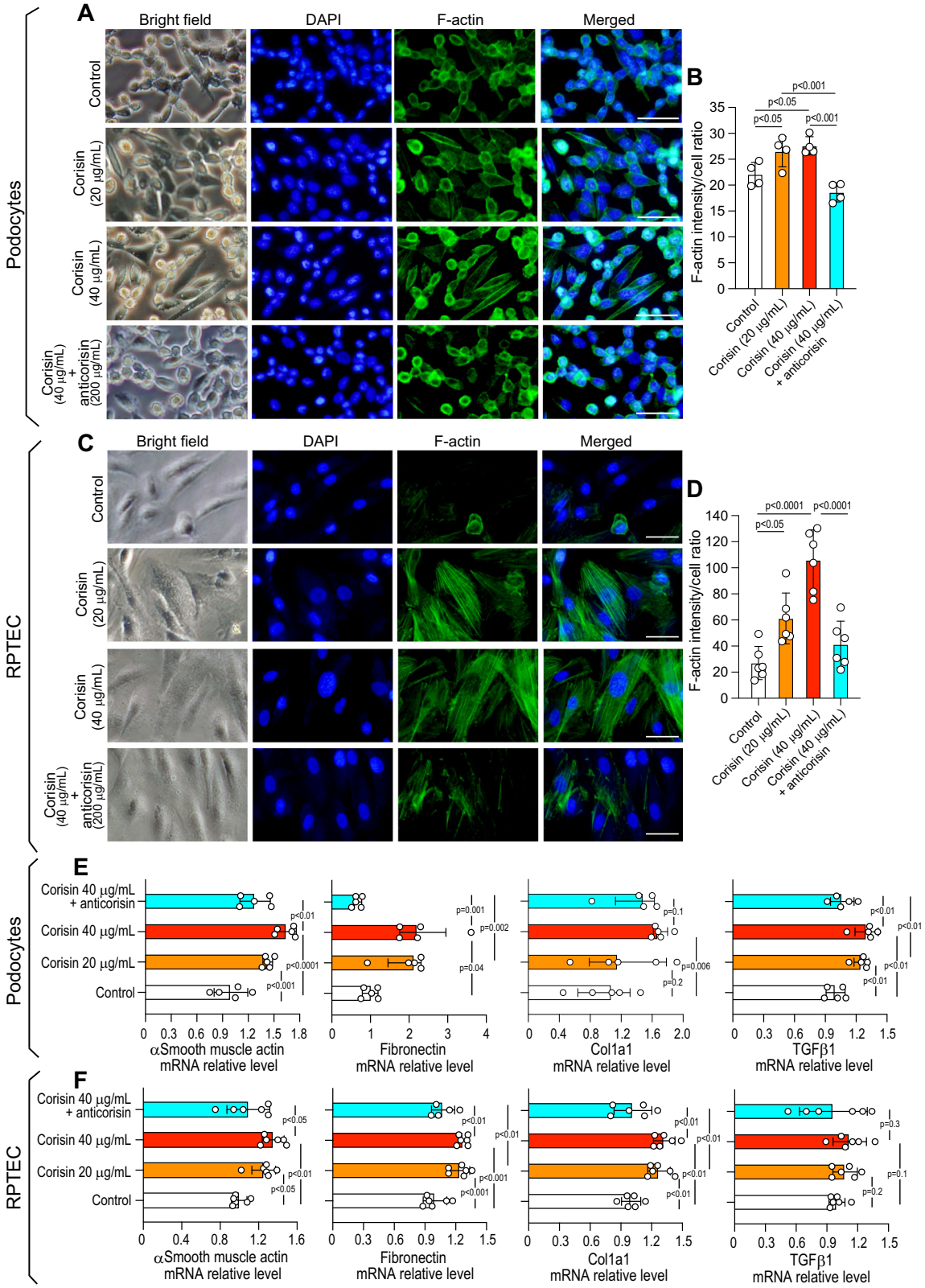

ultimately precipitating a decline in organ function[57,58]. Senescent cells amass in tissues over time, exacerbating fibrosis by releasing an array of pro-inflammatory and profibrotic factors, termed the Senescence-Associated Secretory Phenotype (SASP)[72]. This phenotype includes cytokines, growth factors, and proteases, which perpetuate a chronic inflammatory state, fostering ongoing fibrosis[73]. Such mechanisms underscore senescence as a pivotal factor in the pathogenesis of organ fibrosis, particularly in diabetic CKD. A critical adaptive response enabling cells to circumvent senescence is EMT[60]. This process involves the transformation of epithelial cells into myofibroblasts, which are central to fibrotic tissue remodeling and are prolific producers of collagen[74]. These myofibroblasts may originate from resident epithelial cells, fibroblasts, or circulating fibrocytes, leading to excessive extracellular matrix deposition and scar formation[75,76]. In

Fig. 7 | Corisin induces epithelial-mesenchymal transition in podocytes and renal tubular epithelial cells. A–D Normal human primary podocytes or primary renal proximal tubular epithelial cells (RPTEC) were cultured for 48 h under conditions without corisin (medium containing 0.5% recombinant human albumin) and with corisin at concentrations of 20 and 40 μg/mL, dissolved in 0.5% recombinant human albumin, or 40 μg/mL of corisin with anti-corisin antibody. Subsequently, cells were stained with Phalloidin-iFluor™ 488 and 4′,6-diamidino-2-phenylindole (DAPI). Fluorescence intensity of F-actin and cell counts were quantified using ImageJ, a public domain software from the National Institutes of Health (NIH). $n = 4$ in experiments using podocytes and $n = 6$ in experiments using RPTEC. Scale bars indicate 20 μm. Data are expressed as the mean intensity per cell ratio ± SD. Statistical analysis was performed using ANOVA followed by the Newman-Keuls test; all tests were two-sided. **E, F** Cells were cultured under the same conditions to collect total RNA from each treatment group and assess the mRNA expression of α-smooth muscle actin (*ACTA2*), fibronectin (*FN1*), collagen I (*COL1a1*), and transforming growth factor β1 (*TGFB1*). $n = 5$ in (**E**) and $n = 6$ in (**F**). Normally distributed data are presented as mean ± SD, while skewed data are expressed as the median with interquartile range. Statistical significance was assessed using ANOVA, followed by the Newman-Keuls or Dunn's test; all tests were two-sided. The source data are available in the Source Data file.

diabetic CKD, these fibrogenic processes are intensified by hyperglycemia-induced oxidative stress and the activation of TGFβ signaling pathways, further driving fibrosis[77].

While EMT is well-documented in vitro and has been observed in certain in vivo models, its significance in human CKD remains a subject of considerable controversy[78]. Recent evidence suggests that rather than undergoing a complete transition into myofibroblasts, renal tubular epithelial cells may acquire mesenchymal characteristics and the ability to secrete profibrotic cytokines while remaining attached to the basement membrane, a phenomenon termed partial EMT[79,80]. This concept offers a more nuanced perspective on how epithelial cells contribute to kidney fibrosis while retaining aspects of their epithelial identity. In our current study, we observed that exposure to corisin significantly enhanced markers of cellular senescence, including SAβGal activity and the expression of p16, p21, p27, and p53, while concurrently decreasing the proliferation marker Ki-67. The SASP protein osteopontin levels were notably elevated in human podocytes and primary renal tubular epithelial cells, suggesting that corisin induces senescence in renal cells. Regarding EMT, corisin promoted mesenchymal transformation in vitro in both podocytes and renal tubular epithelial cells, potentially via the secretion of SASP factors. These findings suggest that corisin-associated senescence may contribute to the expansion of collagen-producing cells, although the in vivo significance of this EMT-promoting effect remains to be elucidated. Importantly, most senescence and EMT markers were attenuated by co-treatment with an anti-corisin monoclonal antibody. Additionally, single-cell RNA sequencing analysis of renal proximal tubular epithelial cells reinforced these observations, demonstrating that corisin induces cellular senescence, contributes to the development of a SASP, and enhances myofibroblast-like differentiation. Collectively, these findings suggest that corisin plays a significant role in driving renal fibrosis by promoting cellular senescence and a fibrotic phenotype.

Cellular senescence is a dynamic, heterogeneous, and multistage process regulated by multiple factors, including cell type, the extent of damage, duration of stress exposure, and the nature of intracellular signaling pathways activated[81,82]. Although it is well established that senescent cells often upregulate anti-apoptotic proteins (e.g., members of the BCL-2 family) as a survival mechanism under chronic stress, this is not universally observed across all cell types or stages of senescence[81,83]. For instance, there is evidence showing that senescent fibroblasts are resistant to apoptotic stimuli than their younger counterparts, despite expressing low levels of BCL-2 proteins[84]. Conversely, vascular endothelial cells exhibit increased susceptibility to apoptosis during senescence[85] associated with increased activation of ROS-associated signaling pathways[86], and with reduced Bcl-2 expression alongside elevated levels of the pro-apoptotic protein Bax[87]. In our study, stimulation with corisin elicited hallmarks of both senescence and apoptosis. Specifically, human podocytes and renal tubular epithelial cells displayed elevated expression of senescence markers, including p21 and SAβGal. Concurrently, corisin exposure for 24 and 48 h led to a marked reduction in Bcl-2 and survivin levels, accompanied by increased apoptotic cell death. Flow cytometric analysis supported this dual response, revealing both G0/G1 phase arrest, characteristic of senescence, and an increased proportion of cells in the S and subG1 phases, the latter often reflecting DNA fragmentation associated with apoptosis. These findings suggest that corisin induces a hybrid stress phenotype that engages both senescence- and apoptosis-related signaling pathways, mirroring cellular responses previously described in endothelial cells under prolonged stress. Depending on the nature and intensity of the insult, cells may activate both programs in parallel, with the ultimate fate determined by the balance of pro-survival and pro-death signals[81]. Furthermore, our single-cell transcriptomic analysis revealed that cells with high p21 expression did not uniformly express pro-apoptotic markers, indicating the existence of distinct subpopulations, some undergoing apoptosis and others entering senescence. This observation raises the possibility that corisin induces sufficient stress to trigger apoptosis in one subset of cells while priming another for senescence. Future time-course studies and deeper single-cell analyses will be essential to delineate the temporal dynamics and molecular regulators governing these divergent cell fates.

Albumin is essential for the transport and distribution of various substances, including microbial metabolites, within the human body. It binds to and carries protein-bound substances, ensuring their movement between different body compartments, which is vital for maintaining physiological homeostasis[88,89]. Albumin facilitates the transport of hormones, metals, and fatty acids by binding to specific sites, making it a key player in the body's regulatory mechanisms[89]. Additionally, it is involved in the transport of drugs and toxic substances, significantly influencing their pharmacokinetics and toxicokinetics[90]. Albumin may also carry substances into cells through its various receptors[91]. In our present study, utilizing molecular dynamics simulations and validation experiments, we found that corisin interacts with human albumin, suggesting serum albumin as a potential carrier of corisin. This interaction improves the structural conformation of corisin and enhances its pro-apoptotic activity against podocytes and renal tubular epithelial cells. Moreover, we detected corisin-albumin complexes in the urine of diabetic patients with CKD, supporting the role of albumin in transporting corisin to the intratubular spaces of the kidneys under diabetic conditions. Albuminuria is a well-recognized marker of CKD progression, particularly in patients with diabetic nephropathy[92–94]. Once albuminuria develops, kidney function declines more rapidly[92–94]. While the underlying mechanism remains unclear, evidence suggests that albuminuria induces cytotoxic effects on tubular epithelial cells and podocytes, leading to apoptosis, inflammation, fibrosis, and subsequent nephron damage, ultimately exacerbating kidney dysfunction[51–53]. Our findings suggest that corisin, when bound to albumin, may partly contribute to the toxic effects associated with albuminuria in diabetic patients with CKD. Albumin receptors may facilitate the entry of albumin-bound corisin into podocytes and proximal renal tubular epithelial cells, further exacerbating cellular injury (Fig. 10). Specifically, we identified cubilin, an albumin receptor highly expressed in kidney cells and crucial for albumin reabsorption in tubular epithelial cells, as a mediator of corisin penetration into kidney cells[95–97]. This suggests that cubilin may be a critical contributor to cell injury in diabetic nephropathy. Collectively, our results indicate that albumin and its receptor cubilin play pivotal roles in facilitating corisin's entry into kidney cells

https://doi.org/10.1038/s41467-025-61847-2

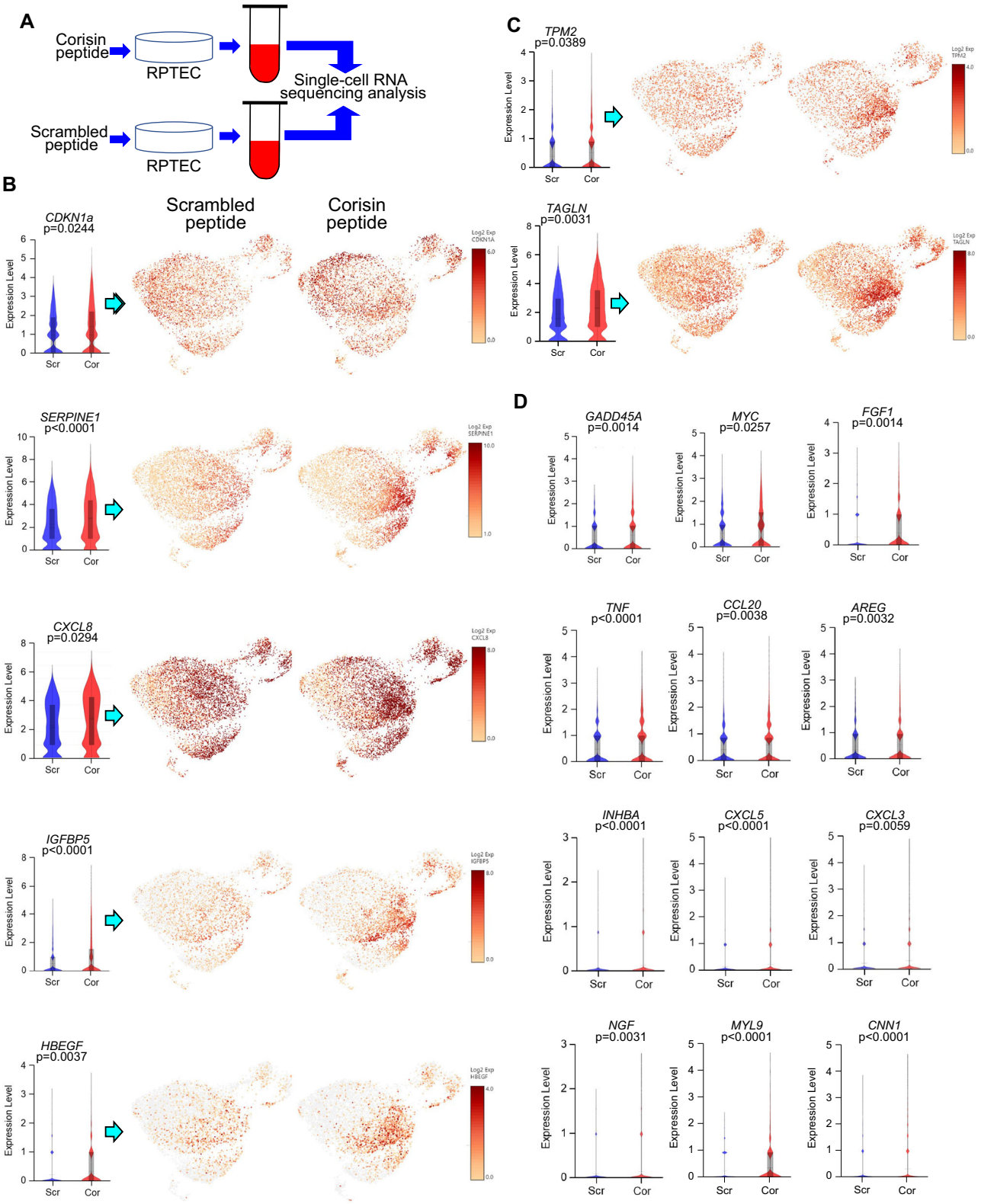

and promoting intracellular damage, thereby accelerating kidney injury and fibrosis in diabetic nephropathy. Further research into the interactions between albumin, cubilin, and corisin may offer novel therapeutic avenues for preventing or slowing kidney disease progression in diabetic patients.

Upon cellular entry, the precise intracellular molecular mode of action of corisin remains incompletely understood. However, our previous investigations demonstrated that corisin induces apoptosis through mitochondrial dysfunction and activation of the intrinsic apoptotic pathway. Specifically, corisin treatment leads to increased accumulation of reactive oxygen species (ROS), mitochondrial membrane depolarization, and activation of proapoptotic factors. Moreover, our earlier research revealed that corisin promotes p53 phosphorylation, a key regulator that governs both apoptosis and senescence. Building on these findings, the present study establishes that corisin accelerates cellular senescence. Given that mitochondrial

Fig. 8 | Corisin induces the expression of senescence-associated factors in primary renal proximal tubular epithelial cells. A Renal proximal tubular epithelial cells (RPTEC) were cultured for 24 h in the presence of corisin or scrambled peptides and subsequently subjected to single-cell RNA sequencing analysis. **B** Violin plots and Uniform Manifold Approximation and Projection (UMAP) plots depict the expression of senescence markers and senescence-associated secretory phenotype (SASP) components in corisin- and scrambled peptide-treated cells. Statistical analysis was conducted using a two-sided Mann–Whitney U test. **C** Violin plots and UMAP plots illustrating the expression of epithelial-mesenchymal transition (EMT) markers in corisin- and scrambled peptide-treated cells. Statistical analysis was conducted using a two-tailed Mann-Whitney U test. **D** Additional senescence, SASP, and EMT markers in corisin- and scrambled peptide-treated cells. Statistical analysis was conducted using a two-sided Mann-Whitney U test. For panels **B, C**, and **D**, single-cell RNA sequencing was performed using three independent RPTEC cultures per stimulant, yielding 9327 high-quality cells for the corisin-treated group and 8186 cells for the scrambled peptide (control) group. Violin plots in (**B**–**D**), represent the distribution of gene expression values. The width of each violin corresponds to the kernel density estimation. The thick vertical bar within each violin denotes the interquartile range (25th-5th percentile), and the thin line (whisker) extends to the minimum and maximum values within 1.5 times the interquartile range. The median is not explicitly displayed.

dysfunction and oxidative stress are well-recognized drivers of cellular senescence and that p53 plays a dual regulatory role in apoptosis and senescence via p21 modulation, our current findings, demonstrating elevated expression of senescence-associated markers, including p21 and p53, strongly suggest that corisin-induced cellular stress and mitochondrial dysfunction contribute to senescence-related pathways. Nonetheless, further investigations are essential to conclusively determine whether corisin-mediated mitochondrial dysfunction and oxidative stress actively drive senescence and influence long-term cellular outcomes.

The present study has several limitations. First, the clinical component was based on a relatively small patient cohort from a single center, which may limit the generalizability of the findings. Second, the specific or additive contribution of corisin could not be clearly distinguished from that of other uremic retention solutes and toxins known to contribute to fibrogenic processes. Third, we did not investigate the potential involvement of corisin-producing bacteria at other mucosal sites, such as the lungs or skin, which may also influence systemic corisin levels. Finally, the mechanistic understanding of the downstream signaling pathways through which corisin promotes fibrosis remains incomplete. Nonetheless, the findings presented in this study provide a strong foundation for future investigations to define the precise role of corisin in kidney fibrosis and assess its potential as a novel therapeutic target.

In conclusion, this study highlights the critical role of corisin in the progression of diabetes-associated kidney fibrosis. Our findings demonstrate that corisin is significantly upregulated in patients with diabetic CKD and in animal models of kidney fibrosis, correlating strongly with disease severity and renal dysfunction. Corisin enhances kidney fibrosis through its interaction with human serum albumin, which facilitates its transport to the kidneys. This interaction promotes cellular senescence and induces EMT, mechanisms central to the progression of kidney fibrosis. Importantly, our therapeutic intervention using an anti-corisin monoclonal antibody significantly improved renal function and halted fibrosis in diabetic mice, underscoring corisin's potential as a novel therapeutic target (Fig. 10). These novel insights could lead to innovative treatments that mitigate renal deterioration and improve patient outcomes in diabetic nephropathy, a significant worldwide health burden.

Methods

Patients

This cross-sectional study included 35 patients with diabetic chronic kidney disease (CKD) who presented to our institutions between June and December 2023. Inclusion criteria consisted of a diagnosis of DM and CKD. Patients undergoing anticancer treatment and those with incomplete data or insufficient sample quality were excluded from the study (Fig. 1A). Supplementary Table 1 summarizes the patients' demographics, clinical characteristics, underlying medical conditions, treatments, and routine laboratory data. The diagnosis and management of DM followed the criteria recommended by the American Diabetes Association (ADA)[98]. The diagnosis and classification of CKD adhered to the Kidney Disease: Improving Global Outcomes (KDIGO) guidelines[99,100]. Blood and urine samples were obtained from all patients and centrifuged, and the serum and urine supernatants were collected and stored at -80 °C until analysis. Five patients (2 males and 3 females; mean age ± SD: 51.4 ± 9.4 years) with non-diabetic chronic kidney disease (CKD) were also included as disease controls. The underlying etiologies of CKD were arterial hypertension (3 cases), hyperuricemia with obesity (1 case), and hemolytic uremic syndrome (1 case). Of these patients, four were classified as stage G3 and one as stage G5, with a mean eGFR of 37.1 ± 18.5 mL/min/1.73 m². In addition, serum samples from 20 healthy volunteers and urine samples from 5 healthy volunteers were included as healthy controls.

Human kidney sections

Formalin-fixed, paraffin-embedded human kidney sections were obtained from OriGene, including samples from patients with chronic kidney disease and those with normal histology. These sections were used for immunostaining of p21, corisin, and assessment of DNA fragmentation.

Animals

Male wild-type (WT) C57BL/6 J mice (Nihon SLC, Hamamatsu, Japan) and TGFβ1 transgenic (TG) mice with a C57BL/6 J background, which naturally develop progressive and fatal kidney fibrosis, were utilized in the experiment[31]. The mice, aged 8–9 weeks, weighed between 20 and 26 g. The TGFβ1 transgenic (TG) mouse model, on a C57BL/6 J background, was specifically engineered to overexpress the full-length human TGFβ1 gene in glomerular podocytes under the control of the mouse podocin promoter[31]. The TG mouse was generated by preparing a chimeric podocin-TGFβ1 bacterial artificial chromosome (BAC) transgenic construct, which contained the full-length coding exons and intervening introns of the human TGFβ1 gene, replacing the mouse podocin gene locus via BAC-mediated recombination and genetic engineering[31]. The transgenic mouse line was established by pronuclear injection of the chimeric construct into C57BL/6 J mouse embryos, and transgenic founders were verified by Southern blot analysis[31]. All experimental animals were bred and housed in a specific pathogen-free environment, maintained at a temperature of 21 °C with a 12-hour light/dark cycle, within the experimental animal facility of Mie University. Each mouse cage was equipped with wood-wool nesting material, and the animals had free access to water and food. Genotyping of the TG mice was performed using standard PCR analysis with DNA extracted from tail samples and specific primer pairs[31].

Ethical statement

All subjects participating in the clinical investigation provided written informed consent, and the study protocol was approved by the Ethical Committees for Clinical Investigation of Mie University (approval No: H2021-029, approval date: 2021/02/09) and conducted following the Principles of the Declaration of Helsinki. Written informed consent was obtained from all participants. This study complies with ethical standards, with efforts to ensure an inclusive design across sex and age, equitable contributions across geographical backgrounds, and data analysis that considers relevant biological and social factors. The Recombinant DNA Experiment Safety Committee (approval No: I-744,

https://doi.org/10.1038/s41467-025-61847-2

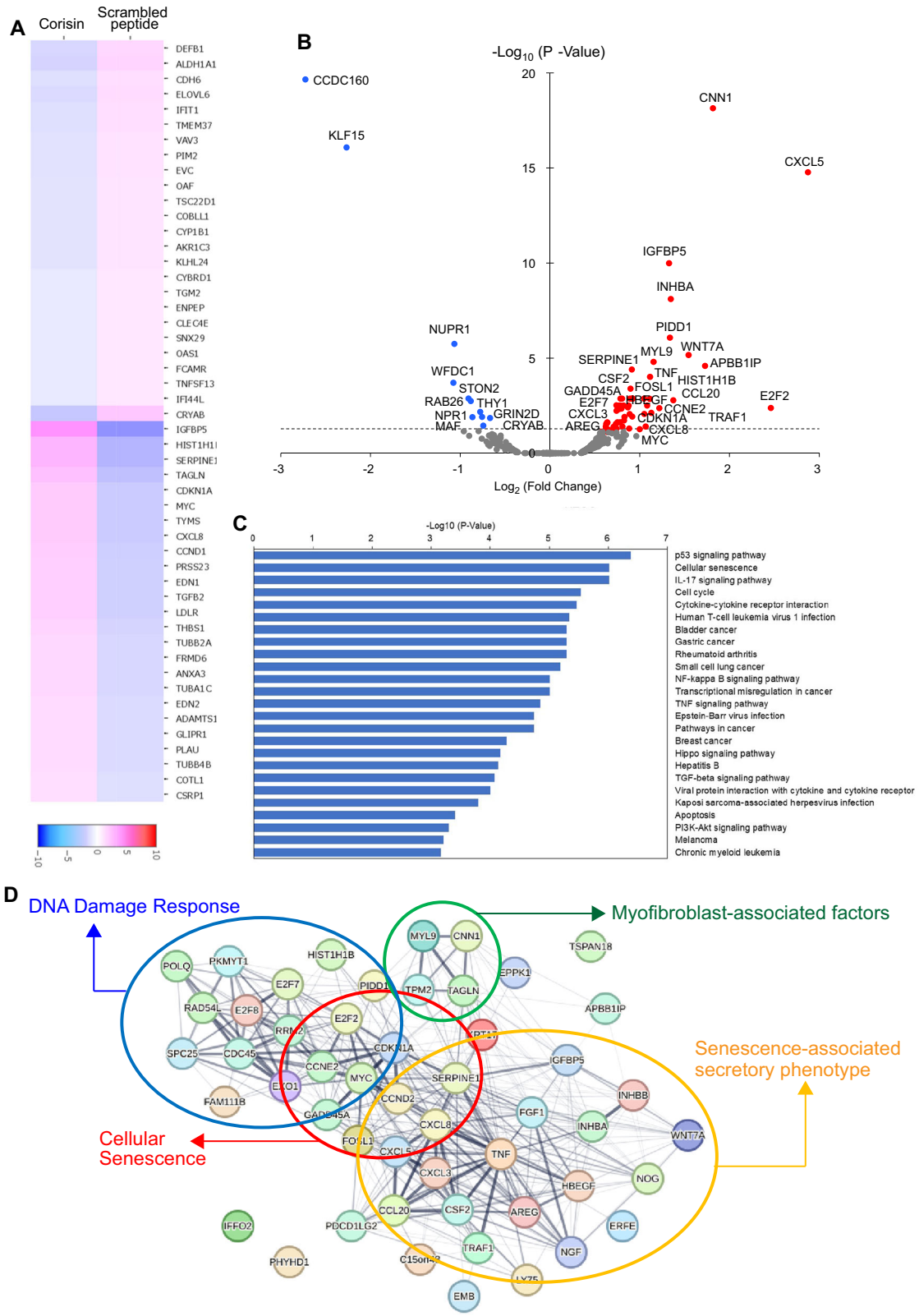

approval date: 2022/11/26; approval No: I-629, approval date: 2023/08/09) and the Committee for Animal Investigation of Mie University approved the experimental protocols (approval No: 2023-17, approval date: 2024/01/09; approval No: 30-14, approval date: 2023/09/04; approval No: 29-23-sai3-h1, approval date: 2023/09/04). We performed all experimental procedures following internationally approved laboratory animal care principles published by the National Institute of Health (https://olaw.nih.gov/). The research followed the ARRIVE Guidelines for animal investigation, and variables were measured blindly of the treatment groups.

Reagents

The clear cell renal carcinoma (Caki-2) cell line, derived from the epithelium of the proximal tubules, and human primary podocytes were

https://doi.org/10.1038/s41467-025-61847-2

Fig. 9 | Corisin stimulation in primary renal proximal tubular epithelial cells promotes pathways associated with the DNA damage response, cellular senescence, the senescence-associated secretory phenotype (SASP), and myofibroblast-like differentiation. A Heatmap showing gene expression in cells stimulated with corisin or a scrambled peptide control. **B** Volcano plots showing differentially expressed genes between corisin- and scrambled peptide-treated renal proximal tubular epithelial cells (RPTEC), based on single-cell RNA sequencing. Each point represents a gene, with the x-axis showing the $\log_2$ fold change and the y-axis showing the $-\log_{10}$ adjusted *p*-value. Differential expression analysis was performed using a two-tailed Mann–Whitney U test. Since gene expression was assessed across thousands of genes, *p*-values were adjusted for multiple comparisons using the Benjamini-Hochberg method to control for the false discovery rate. **C** Kyoto Encyclopedia of Genes and Genomes (KEGG) pathway enrichment analysis reveals significant overrepresentation of pathways related to cellular senescence in corisin-treated renal proximal tubular epithelial cells. Enrichment analysis was performed using the hypergeometric test, and *p*-values were adjusted for multiple comparisons using the Benjamini-Hochberg method to control the false discovery rate. **D** Categorization of differentially expressed genes by their biological roles, demonstrating their involvement in various cellular processes.

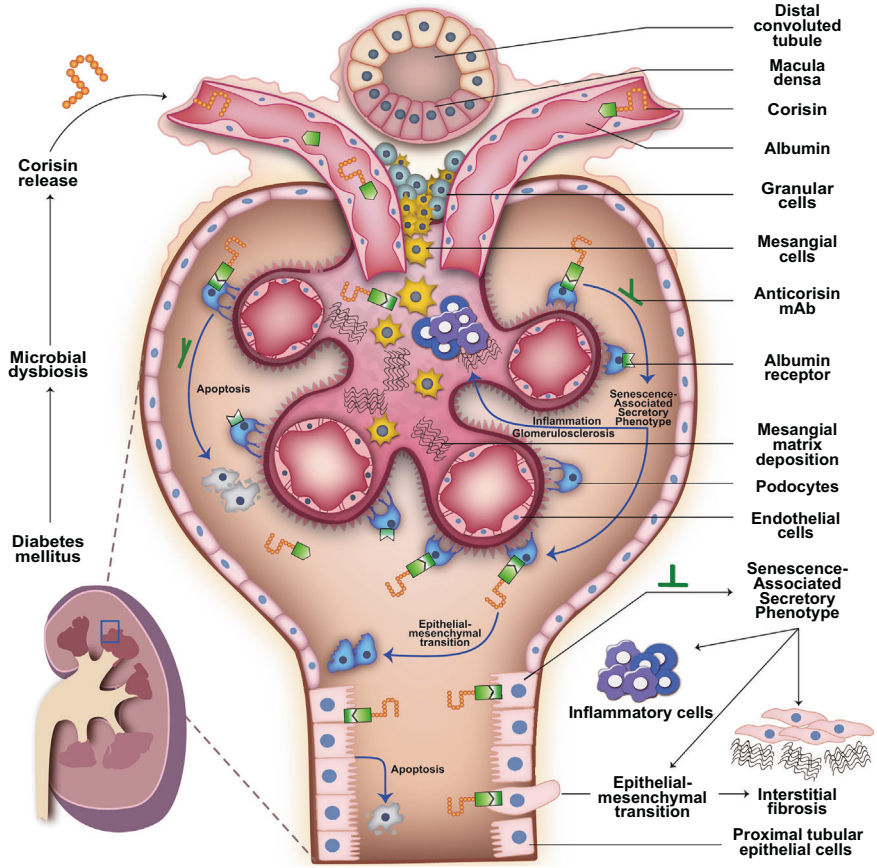

Fig. 10 | Corisin-induced kidney cell damage and fibrosis in diabetic chronic kidney disease and the protective potential of anticorisin monoclonal antibody. Diabetes-associated dysbiosis increases corisin release from the microbiome into systemic circulation, where it binds to serum albumin. The corisin-albumin complex reaches the glomeruli and proximal tubular epithelial cells, binding to cubilin, an albumin receptor, and thereby facilitating corisin entry into podocytes and proximal tubular epithelial cells. Within these cells, corisin induces a senescence-associated secretory phenotype, resulting in the elevated secretion of inflammatory cytokines, chemokines, matrix metalloproteinases, and growth factors that promote inflammation, epithelial-mesenchymal transition, apoptosis of podocytes and tubular epithelial cells, myofibroblast recruitment, and extracellular matrix deposition (e.g., collagen I). Areas of the glomeruli and tubules affected by increased apoptosis are subsequently replaced by fibrotic tissue, accelerating disease progression and leading ultimately to a fatal outcome. The anti-corisin monoclonal antibody binds to corisin peptides, blocking their pro-senescence activity and mitigating disease progression. mAb, monoclonal antibody.

obtained from the American Type Culture Collection (Manassas, VA), while human renal primary tubular epithelial cells (RPTEC) were sourced from LONZA (Houston, TX). RPMI 1640 medium (RPMI) was acquired from Nacalai Tesque (Kyoto, Japan), while fetal bovine serum (FBS) was obtained from Bio Whittaker (Walkersville, MD). L-glutamine, penicillin, and streptomycin were procured from Invitrogen (Carlsbad, CA). Synthetic corisin and its corresponding scrambled peptide were synthesized and supplied by Peptide Institute Inc. (Osaka, Japan) and Thermo Fisher Scientific (Waltham, MA).The siRNAs against each albumin receptor were purchased from Origene (Rockville, MD, USA). Fluorescein isothiocyanate (FITC)-labeled corisin and FITC-labeled scrambled peptide were also from Peptide Institute Inc. (Osaka, Japan), and MitoTracker™ Red CMXRos was from Thermo Fisher Scientific (Waltham, MA).

Evaluation of corisin interaction with recombinant human albumin

Mixtures of 20 µg recombinant human albumin with several amounts of synthetic corisin or synthetic scrambled peptide were prepared in saline and incubated at 37 °C. The mixture was thoroughly mixed by pipetting, centrifuged, and incubated at 94 °C for 5 min. The samples were then loaded onto a 10-20% SDS-polyacrylamide gel electrophoresis (SDS-PAGE) gel. Subsequently, Western blotting was performed using anticorisin mAb 21 A or anti-albumin antibody.

Evaluation of the interaction between corisin and human serum albumin

Serum samples from patients with diabetic nephropathy and healthy controls were diluted at a ratio of 1:20 and incubated for 10 min with corisin (4 μg) diluted in saline. As a control, a mixture containing corisin (4 μg) and recombinant human albumin (rhAlb, 5 μg) was also prepared. Each mixture was subsequently subjected to electrophoresis, followed by Western blot analysis using monoclonal antibodies specific to corisin or albumin.

Evaluation of the pH-dependent interaction between corisin and human serum albumin

Serum samples from patients with diabetic nephropathy and healthy controls were diluted 1:20 and incubated for 10 min with or without 10 μg of corisin in saline solutions adjusted to various pH levels using hydrochloric acid. In a separate experiment, 2.5 μg of recombinant human albumin (rhAlb) was incubated with 3 μg of corisin in saline under different pH conditions. Each mixture was then subjected to electrophoresis and analyzed by Western blotting using monoclonal antibodies specific for corisin or human albumin.

Gel band excision for mass spectrometry analysis

A mixture of corisin and rhAlb in a saline solution and a control sample containing rhAlb alone were prepared. The mixtures were thoroughly mixed by pipetting, centrifuged, and incubated at 94 °C for 5 min. Subsequently, the samples were subjected to 10–20% SDS-PAGE. Upon completion of electrophoresis, the gel was carefully removed, briefly rinsed with distilled water, and then immersed in a fixative solution with agitation for 30 min. Following fixation, the gel was transferred to a Coomassie blue staining solution and agitated for approximately 2 h to visualize the protein bands. The gel was then destained, and images were captured. Bands of interest were excised from the gel using a sterile scalpel for subsequent mass spectrometry analysis.

Mass spectrometry to determine co-localization of corisin with recombinant human albumin

Proteomic analyses were performed at the Proteomics Core Facility of the Roy J. Carver Biotechnology Center at the University of Illinois Urbana-Champaign. Excised gel bands were cut into 1 mm cubes and de-stained thrice with 50% acetonitrile in 50 mM triethylammonium bicarbonate. The gel pieces were then dehydrated with acetonitrile and swelled with 150 μL of 50 mM triethylammonium bicarbonate containing 1 μg of mass spectrometry-grade trypsin (Pierce). The samples were digested overnight at 37 °C, and on the following day, the digested peptides were extracted three times with 50% acetonitrile in 5% formic acid. The samples were dried in a speed vac, desalted with StageTips,1, and then dried again.

The peptides were resuspended in 15 μL of 5% acetonitrile in 0.1% formic acid, and 1 μL of each sample was injected into an UltiMate 3000 RSLCnano system coupled to an Orbitrap Fusion mass spectrometer (Thermo Fisher Scientific). Peptide separation was performed using a 25 cm Acclaim PepMap 100 C18 column (Thermo Fisher Scientific) maintained at 50 °C, with mobile phases consisting of 0.1% formic acid in water (A) and 0.1% formic acid in acetonitrile (B). The gradient elution was carried out over 45 min from 2% to 36% B at a flow rate of 300 nL/min, followed by column washing and equilibration. The mass spectrometer operated in positive ion mode. MS1 (first-stage mass analysis) scans were acquired over a range of 300–2000 m/z at a resolution of 120,000. The most abundant ions detected in MS1 scans were subjected to CID (collision-induced dissociation) fragmentation with a normalized collision energy of 35%, and MS2 (second-stage mass analysis) scans were acquired in the ion trap, with a total cycle time of 3 s. The isolation window was set at 1.6 m/z, and dynamic exclusion was applied with a duration of 60 s.

Raw LC-MS data were analyzed using Mascot Distiller v.2.8.4.0 and an in-house Mascot server v.2.8.2 (Matrix Science). Database searches were performed against the Homo sapiens reference proteome from UniProt (104,451 entries) and a custom FASTA file containing the sequences of corisin and the scrambled peptide. Search parameters included a peptide mass tolerance of 10 ppm, a fragment mass tolerance of 0.6 Da, and allowance for up to two missed tryptic cleavages. Protein identifications were filtered in Mascot using the default significance threshold of $p < 0.05$.

Co-immunoprecipitation of corisin with human albumin

A preparation containing 5 μg of recombinant human albumin and 50 ng of corisin was constituted in 20 μL of Tris-buffered saline (TBS) and subsequently incubated at 37 °C for 30 min. Following this, 2 μg of anti-corisin monoclonal antibody (mAb) at a concentration of 1 mg/mL was introduced to the solution and incubated at 4 °C for an additional 30 min. Protein G agarose beads (10 μL) were added, and the mixture was further incubated for 30 min at 4 °C. After the incubation, the beads were meticulously washed three times with TBS to remove any nonspecific interactions. Thereafter, 10 μL of 2x sodium dodecyl sulfate (SDS) loading buffer was added to the beads to elute the proteins, followed by centrifugation to separate the supernatant. The eluted proteins' supernatant was then applied to a 10-20% SDS-PAGE. Post-electrophoresis, Coomassie blue staining was employed to analyze the protein complexes resultant from the co-immunoprecipitation procedure.

Cell culture

All cells were cultured in RPMI 1640 medium, enriched with 10% fetal calf serum, 0.03% (w/v) L-glutamine, 100 IU/ml penicillin, and 100 μg/ml streptomycin. The cultures were maintained in a controlled environment featuring a 5% CO_2 atmosphere at a constant temperature of 37 °C.

Cell stimulation with corisin

Given corisin's interaction with albumin and its stability in the presence of albumin, unless otherwise specified, all in vitro cell assays were performed using corisin diluted in a solution containing recombinant human albumin, unless otherwise specified. While the serum albumin concentration in human plasma is typically 35-50 g/L (~3.5–5% w/v), we used 0.5% HSA as a physiologically relevant lower-bound concentration to approximate albumin levels in the renal tubular microenvironment, particularly under pathological conditions such as diabetic nephropathy where proteinuria leads to albumin leakage into the tubular lumen. In our experimental setup, the apical side of the tubular epithelial cells faced the medium, simulating luminal (urinary) exposure, where corisin could be present in proteinuric states.

Apoptosis assay

To assess apoptosis, cells (4 × 105 cells/well) were cultured in 12-well plates until they reached subconfluency. Subsequently, they were serum-starved for 12 h and then exposed to stimulants for 48 h. Apoptosis was quantified by flow cytometry (FACScan, BD Biosciences, Oxford, UK) using fluorescein-labeled annexin V and propidium iodide (FITC Annexin V Apoptosis Detection Kit with PI, Biolegend, San Diego, CA). The gating strategy is shown in Supplementary Fig. 26. Apoptosis was also evaluated using the terminal deoxynucleotidyl transferase dUTP nick end labeling (TUNEL) assay, which was conducted at MorphoTechnology Corporation in Sapporo, Hokkaido, Japan, following standard protocols.

Flow cytometric analysis of cell cycle

Cells were harvested using trypsin/EDTA and washed once with phosphate-buffered saline (PBS). Following centrifugation, the cell pellet was vortexed thoroughly. To fix the cells, cold 70% ethanol was added dropwise to the pellet while vortexing to prevent clumping. The cells

were then incubated in ethanol at 4 °C for 60 min. After fixation, the cells were washed twice with PBS by centrifugation at 850 × g, and the supernatant was discarded. The resulting pellet was resuspended, and cells were treated with ribonuclease by adding 50 µl of RNase A (from a 100 µg/ml stock solution). Subsequently, 200 µl of propidium iodide (PI) was added from a 50 µg/ml stock solution for DNA staining. For flow cytometric analysis, forward scatter (FSC) and side scatter (SSC) were measured to identify single-cell populations. To exclude cell doublets, pulse processing was performed by analyzing PI-Area versus PI-Width.

Cell proliferation assay

Cells were seeded at a density of 1×10^4 cells per well in 100 µL of culture medium in a 96-well plate. The cells were then stimulated with 0, 20, or 40 µg/mL of corisin, with or without the addition of 200 µg/mL of anti-corisin mAb (21 A), and incubated for 24 h at 37 °C in a humidified atmosphere containing 5% CO_2. Following stimulation, 20 µL of CellTiter 96® AQueous One Solution Reagent (Promega Corporation, Madison, MI, USA) was added to each well, and the plate was incubated for an additional 2 h at 37 °C. Cell proliferation was assessed by measuring absorbance at 490 nm using a 96-well plate reader.

Evaluation of nuclear morphology

Primary human podocytes and primary normal human renal tubular epithelial cells were cultured for 48 h in the presence of corisin at concentrations of 20 µg/mL and 40 µg/mL or an equivalent concentration of scrambled peptide as a control. Following incubation, the cells were fixed and stained with 4′,6-diamidino-2-phenylindole (DAPI) to visualize nuclear morphology. Nuclear parameters, including nuclear area, perimeter, and circularity, were quantitatively assessed using ImageJ, an open-source image analysis software. Automated image segmentation and thresholding were applied to ensure consistent measurement of nuclear features.

Evaluation of corisin targeting mitochondria in human renal cells

Human renal tubular Caki-2 cell lines and primary human podocytes were cultured in RPMI-1640 medium supplemented with 10% fetal bovine serum (FBS) at a seeding density of 1 × 104 cells per well. The cells were grown on collagen I-coated 4-well culture slides (Corning 354557, Biocoat) and incubated at 37 °C in a humidified atmosphere with 5% CO_2 overnight. The following day, the culture medium was replaced with RPMI-1640 containing 1% FBS, and incubation continued at 37 °C overnight. Subsequently, the medium was replaced with a solution containing 20 µg/mL of fluorescein isothiocyanate (FITC)-labeled corisin in 0.5% rhAlb or an equivalent dose of FITC-labeled scrambled peptide, and the cells were incubated for 4 h at 37 °C. After incubation, the medium was aspirated, and the cells were washed thrice with phosphate-buffered saline (PBS) devoid of calcium and magnesium to remove residual dye or peptide. Cells were then treated with a 20 nM MitoTracker staining solution to label mitochondria for 30 min at 37 °C, followed by fixation in 4% paraformaldehyde in PBS (without calcium and magnesium) for 10 min at room temperature, and subsequently washed three times with PBS. The nuclei were stained with 1 µg/mL DAPI (4′,6-diamidino-2-phenylindole) in PBS for 5 min at room temperature, followed by additional PBS washes. Visualization was performed using a fluorescence microscope (Olympus Corporation, Tokyo, Japan), and images were captured and analyzed using image processing software.

Evaluation of corisin penetration into renal tubular cells in the absence of albumin

RPTECs were seeded at a density of 2×10^4 cells per well in a 24-well culture plate and allowed to adhere. The culture medium was then replaced with RPMI, either without albumin or supplemented with 0.5% rhAlb. FITC-labeled corisin was added at a final concentration of 40 µg/mL in either saline or 0.5% rhAlb, and the cells were incubated for 4 h at 37 °C. After incubation, the medium was removed, and the cells were stained with 50 nM Mitotracker Red CMXRos, prepared from a 1 mM stock solution in DMSO, followed by a 30-minute incubation at 37 °C. The cells were then washed with PBS (-Ca, -Mg) and fixed with 4% paraformaldehyde (PFA) in PBS (-Ca, -Mg) for 10 min at room temperature. After fixation, the cells were washed twice with PBS (-Ca, -Mg)) and stained with 1 µg/mL DAPI in PBS (-Ca, -Mg) to visualize nuclei, followed by two additional PBS washes. Finally, fluorescence microscopy analysis was performed to assess corisin penetration and mitochondrial localization.

Western blotting

The cells were washed twice with cold phosphate-buffered saline and subsequently lysed in RIPA buffer. This buffer consisted of 10 mM Tris-Cl (pH 8.0), 1 mM EDTA, 1% Triton X-100, 0.1% sodium deoxycholate, 0.1% SDS, 140 mM NaCl, and 1 mM phenylmethylsulfonyl fluoride. Protease/phosphatase inhibitors, including 1 mM orthovanadate, 50 mM β-glycerophosphate, 10 mM sodium pyrophosphate, 5 µg/mL leupeptin, 2 µg/mL aprotinin, and 5 mM sodium fluoride, were also added to the buffer. The resulting mixture was centrifuged at 17,000 x *g* for 10 min at 4 °C, and the protein concentration was determined using the Pierce BCA protein assay kit from Thermo Fisher Scientific Incorporation (Waltham, MA). Samples with equal protein amounts were mixed with Laemmli sample buffer and then separated using SDS-PAGE. For Western blotting, nitrocellulose membranes and anti-corisin mAb were used. The intensity of the bands on the blots was quantified with the NIH ImageJ1.54 m program developed by Wayne Rasband at the NIH Research Service Branch (wayne@codon.nih.gov).

Molecular Dynamics simulation of the conformational ensemble of corisin

Molecular Dynamics simulation (MDS) set-up. Two separate simulation systems were built to observe the conformational ensemble of peptide: the unfolded/extended structure of the peptide, which was constructed in PyMol 2.1 (https://pymol.org/2/), and the folded structure of the peptide, which was built by SWISS-MODEL (https://swissmodel.expasy.org/). The N-terminal of the peptide was capped using the neutral acetyl group (ACE), and the C-terminal was capped using a neutral methylamine group (NME). The peptide was solvated in an orthogonal TIP3P water box, and the systems were neutralized by 150 mM NaCl using Packmol v18.169[101].

All MDS were performed using the Amber18 software package employing Amber ff14SB forcefield. Each MDS system was first minimized for 50000 cycles. The minimization method switched from the steepest descent for the first 5000 cycles to a conjugate gradient for the remaining 45000 cycles. The systems were heated from 0 K to 300 K under the NVT ensemble. The heating step was conducted for 3 ns using a Langevin thermostat with a collision frequency of 2 ps-1. The systems were equilibrated in an NPT ensemble for 2 ns with a pressure of 1 bar using a Monte Carlo barostat. The systems were further equilibrated in an NPT ensemble (300 K and 1 bar) for 50 ns and underwent production runs[102]. The SHAKE algorithm was used to constrain hydrogen-containing bonds[103]. All systems underwent hydrogen mass repartitioning (HMR)[104], which redistributes mass between hydrogen atoms and their covalently bonded heavy atoms within the peptide. This adjustment permits an increase in the simulation timestep to 4 fs.

For two systems, ~20 µs simulation was obtained by applying the adaptive sampling method[105], that was used to efficiently sample the conformational space of the peptide. In this study, the least count-based adaptive sampling was used to find the new conformational states quickly. Adaptive sampling was performed as follows: (1) Run a series of short MDS from a collection of starting structures. (2) Cluster all collected simulation data using the K-means algorithm. The distances of all pairs of residues separated by two or more residues were

used as the reaction coordinates for generating 100 clusters. (3) Randomly pick one state from each of 25 clusters with the least population as seeds to start a new simulation. (4) Repeat steps 1-3 until the sampling reaches convergence.

In adaptive sampling, a bias was introduced as simulations initiated from the least populated states after each round, potentially resulting in a population distribution that deviates from the real equilibrium population of states. To eliminate this sampling bias, a Markov State Model (MSM) was constructed to interconnect all clusters by estimating the transition probability matrix across all conformational states[106–108].

Markov State Model (MSM) Construction. MSM was built by the python package PyEMMA 2.5.6[109]. The distances of all pairs of residues separated by two or more residues were used for featurizing the simulation data, and 136 residue-residue distances were included in the feature matrix. The optimal number of microstates for MSM was selected by maximizing VAMP score[110]. The lag time of 20 ns was chosen from the implied time scale plot and Chapman-Kolmogorov test[111] was performed to validate the Markovian behavior of the MSM.

Transition path theory (TPT). TPT was applied to calculate the transition timescale between different conformational states[112]. The transition time from state A to state B was estimated from mean free passage time (MFPT), which is the inverse of the rate of the reaction ($1/k_{AB}$) calculate by the following equation (1):

$$1/k_{AB} = \tau \sum_{i=1}^{m} \pi_i (1 - q_i^+)/F$$

where τ is lag time of MSM, π_i is the stationary probability of microstate i, F is the total flux between state A and state B, q_iˆ+ is the forward committor probability that when the system is at microstate i, it will reach the state B instead of state A. TPT was performed by the python package PyEMMA 2.5.6[109].

Trajectory analysis. CPPTRAJ module in AMBER (Assisted Model Building with Energy Refinement) 22[42] and the python package MDTraj[113] were used to analyze trajectory data, and VMD 1.9.3[114] and PyMol 2.1 (https://pymol.org/2/) were used to visualize MDS snapshots. The Python package Matplotlib[115] was used to generate the 2-D plot of the free energy landscape.

Definition of Fraction of Native Contacts. Native contacts are interactions between residues that are in contact within the native structure[116]. The fraction of native contacts, denoted as Q, is calculated by the following equation (2):

$$Q(X) = \frac{1}{S} \sum_{(i,j)\in S} \frac{1}{1 + \exp[\beta(r_{ij}(X) - \lambda r_{ij}^0)]}$$

where X is a conformation, $r_{ij}(X)$ is the distance between atom i and j in conformation X, r_{ij}^0 is the distance between heavy atoms i and j in the native conformation, S is the set of all pairs of heavy atoms *(i, j)* belonging to the residue θ^i and θ^j such that $|\theta^i - \theta^j| > 3$ and $r_{ij}^0 < 4.5$ Å, $\beta = 5$ Å^{-1} is a smoothing parameter, $\lambda = 1.8$ for the all-atom model.

Molecular dynamics simulation of corisin interaction with human and bovine albumin

Molecular dynamics simulation set-up. We prepared two systems for MDS: (i) HSA-corisin (Human Serum Albumin-corisin) and (ii) BSA-corisin (Bovine Serum Albumin-corisin). The complex structures of HSA-corisin and BSA-corisin were predicted by AlphaFold-Multimer[40]. The systems were solvated in a TIP3P water box and neutralized by 150 mM NaCl. Amber ff14SB force field was used for protein parameterization. All systems underwent minimization and equilibration first by using Amber 18 software[117]. Each MDS system was minimized for 5000 cycles with the steepest descent algorithm and then further minimized for 45000 cycles with the conjugate gradient algorithm. The temperature of minimized systems was increased from 0 K to 300 K under the NVT (Number of particles, Volume, Temperature) ensemble. Heating steps were performed for 3 ns by using a Langevin thermostat with a collision frequency of 2 ps-1. The heated systems were pressurized to a constant pressure of 1 bar under the NPT ensemble. The pressure of the systems was controlled by using a Monte Carlo barostat. During heating and pressurized steps, the backbone atoms of proteins were restrained with a weight of 5 kcal/mol/Å2. Then, restraints were removed, and systems were further equilibrated for 50 ns in an NPT ensemble (300 K and 1 bar). The production runs were performed using OpenMM[41]. Shake algorithm was used to constrain the hydrogen-containing bonds[103]. Hydrogen mass repartitioning (HMR) was applied to all systems, which redistributes mass between hydrogen atoms and heavy atoms of protein/peptide to allow the time step of the simulation to be increased to 4 fs[104].

Trajectory analysis. CPPTRAJ in Amber 18 was used to process MDS trajectories[42]. Feature calculation and data analysis were performed by the Python package MDTraj[113]. VMD 1.9.3[114] was used to visualize the MDS trajectories.

Linear Interaction analysis. Linear Interaction Energy (LIE)[118] function in CPPTRAJ was used to estimate non-bonded interactions between all-atoms in the ligand and all-atoms in the surroundings. 10 Å was used as a cutoff to determine the surrounding atoms of ligands. The binding free energy was calculated as a linear combination of electrostatics and van der Waals interactions for all-atom pairs based on the following formula (3) (default values: $\alpha = 0.16$, $\beta = 0.5$, $\gamma = 0.0$):

$$\Delta E_{LIE} = \alpha\left(E_{bound}^{vdW} - E_{free}^{vdW}\right) + \beta\left(E_{bound}^{ele} - E_{free}^{ele}\right) + \gamma$$

Induction of exacerbation of kidney fibrosis in TGFβ1 transgenic mice

This experiment was conducted to investigate whether the systemic administration of corisin exacerbates kidney fibrosis. Female TGFβ1 transgenic (TG) mice, aged 9 weeks, were randomly assigned to two treatment groups. A group received intraperitoneal injections of synthetic corisin ($n = 5$) at a dose of 5 mg/kg body weight, administered three times per week for two weeks. Another group ($n = 6$) was administered a synthetic scrambled peptide at the exact dosage and via the same route for two weeks. In a previous study, we demonstrated that administering corisin at a dose of 5 mg/kg every two days for two weeks exacerbated the progression of lung fibrosis. Based on these findings, we adopted a similar dosing regimen in the current experiment, administering six doses over two weeks to ensure sufficient and sustained exposure to corisin while assessing its effects on the worsening of kidney fibrosis. Plasma and urine samples were collected on Days 1, 8, and 15 from both groups to assess kidney function. On Day 16, euthanasia was performed, followed by the final collection of blood, urine, and kidney tissues.

Induction of DM in TGFβ1 TG mice with kidney fibrosis

DM was induced in WT and TGFβ1 TG mice through intraperitoneal administration of streptozotocin (STZ) (Sigma, St. Louis, MO) at a dose of 40 mg/kg body weight for five consecutive days. Mice that received an equivalent volume of sterile physiological saline (SAL) via intraperitoneal injection served as controls. Blood glucose levels were assessed in the fourth week post-STZ administration. DM was confirmed through a glucose tolerance test. Mice with blood glucose levels

exceeding 200 mg/dL were classified as diabetic. Diabetic and non-diabetic TGFβ1 TG mice were euthanized at week nine following STZ administration, and blood, urine, and kidney tissue samples were collected for further analysis.

Induction of diabetic nephropathy in WT mice

To expedite the onset of DM-associated nephropathy, a group of wild-type mice underwent unilateral nephrectomy followed by STZ administration. The procedure was performed under deep anesthesia in sterile conditions. A surgical incision was made along the right dorso-lumbar region, allowing visualization of the ureter and renal artery. Both structures were carefully ligated, and the kidney was excised at the proximal region near the renal hilum. The incision was then sutured, and the mice were allowed to recover for four weeks. After complete recovery, the mice received intraperitoneal injections of STZ at a dose of 40 mg/kg body weight for five consecutive days to induce DM. Control mice were administered an equivalent volume of sterile physiological saline under identical conditions. Blood samples were collected in the fourth-week post-STZ injection to measure glucose levels. Mice with blood glucose levels exceeding 200 mg/dL were classified as diabetic and included in the study cohort. Four weeks after DM diagnosis, the mice were humanely sacrificed under deep anesthesia, and blood and kidney tissue samples were collected for further analysis. To assess the degree of fibrosis in each mouse group, Masson's trichrome staining was performed on formalin-fixed, paraffin-embedded tissue sections, and the extent of fibrosis was quantified using WinROOF imaging software.

Evaluation of the therapeutic effect of a neutralizing anticorisin mAb in diabetic TGFβ1 TG mice with kidney fibrosis

This experiment aimed to investigate the effects of anticorisin treatment in diabetic TGFβ1 TG mice with kidney fibrosis. TGFβ1 TG mice typically develop renal dysfunction as early as 8 weeks of age, compared to their WT counterparts[31]. However, this renal dysfunction remains relatively stable for several weeks before progressing to a fatal stage. To minimize early mortality during the experimental period, human TGFβ1 TG mice with relatively mild renal dysfunction were selected for DM induction, enabling the observation of disease exacerbation while reducing the risk of premature death. DM was induced in the TGFβ1 TG mice by intraperitoneal injections of streptozotocin (STZ) (Sigma, St. Louis, MO). STZ was administered at a dosage of 40 mg/kg body weight for five consecutive days. A negative control group of WT mice was administered an equivalent volume of saline (SAL) intraperitoneally. DM induction was confirmed by a non-fasting blood glucose level of 200 mg/dL or higher and by an intraperitoneal glucose tolerance test. Following DM induction, the mice were assigned to three groups: (1) TGFβ1 TG mice treated with anticorisin mAb ($n = 5$), (2) TGFβ1 TG mice treated with control immunoglobulin G (IgG) ($n = 5$), and (3) wild-type (WT) mice as a negative control ($n = 4$). The treatment phase began in the fifth week, where the mice received intraperitoneal injections of either anticorisin mAtb or control IgG at a dose of 10 mg/kg three times per week for eight weeks. The reported half-life of the anti-corisin mAb is approximately three days. To maintain a steady antibody level, minimize significant troughs in its concentration, and evaluate its efficacy, we administered three doses per week for eight weeks[29]. At the end of the 13-week experimental period, the mice were sacrificed, and samples of blood, urine, and kidneys were collected for further analysis to evaluate the impact of anticorisin treatment on kidney fibrosis.

Specimen collection and handling procedures

The animals were euthanized by intraperitoneal injection of an overdose of 5% isoflurane. Following euthanasia, samples were collected for biochemical analysis and histological staining. Blood was obtained via closed-chest cardiac puncture and collected into tubes containing 10 U/mL heparin as an anticoagulant. Urine samples were gathered using metabolic cages. After systemic circulation was flushed with physiological saline, each kidney was dissected, isolated, and weighed. The left kidney was stored at -80 °C for subsequent analysis, while the right kidney was fixed in 10% paraformaldehyde, dehydrated, embedded in paraffin, and sectioned into 3-μm thick slices for staining with hematoxylin and eosin (H&E), periodic acid-Schiff (PAS), or Masson's trichrome. Images of the resected kidneys were captured using an Olympus BX53 microscope equipped with a digital camera (Olympus DP73, Tokyo, Japan). Glomerular sclerosis was evaluated based on PAS staining. For each mouse, 25 glomeruli were randomly selected and scored as follows: 0 for normal glomeruli, 1 for mild mesangial thickening (PAS-positive area <25%), 2 for moderate segmental sclerosis (PAS-positive area 25–50%), 3 for severe segmental sclerosis (PAS-positive area 50–75%), and 4 for global sclerosis (PAS-positive area ≥75%). The mean score from the 25 glomeruli was defined as the glomerular sclerosis score. Six investigators, blinded to the treatment groups, performed the scoring. Renal fibrosis was assessed using Masson's trichrome staining. Ten images of the kidney cortex per mouse were randomly acquired, and the ratio of Masson's trichrome-positive area to the total kidney cortex area was calculated using WinROOF image processing software (Mitani Corp., Fukui, Japan).

Evaluation of diabetes status and kidney functional parameters

Non-fasting blood glucose levels were periodically monitored to assess the diabetic state. The glucose tolerance test was conducted by intraperitoneal injection of glucose at a dose of 1 g/kg following overnight fasting, with blood glucose levels measured at 0, 15, 30, 60, and 120 min. Blood glucose levels were determined using the glucose oxidase method with a glucose assay kit (Dojindo, Mashiki, Japan). Blood albumin levels were measured using the A/G B test (Wako, Osaka, Japan), and urinary albumin levels were assessed using the Mouse Urine ELISA Kit (Exocel, San Diego, USA). Blood creatinine levels were measured using the Mouse Creatinine Kit (Crystal Chem, Elk Grove Village, USA), urinary creatinine levels were determined using the Creatinine Companion Kit (Exocel, San Diego, USA), and blood urea nitrogen levels were measured using the Urea Nitrogen Detection Kit (Arbor Assays, Ann Arbor, USA).

Immunohistochemical staining

Staining for corisin was performed using an in-house anti-corisin monoclonal antibody (clone A21; dilution 1:300), and commercially available antibodies against p21 (cat. no. sc-6246; dilution 1:50; Santa Cruz Biotechnology, Dallas, TX, USA), F4/80 (cat. no. 28463-1-AP; dilution 1:1200; Proteintech, Rosemont, IL, USA), and p53 (cat. no. ab131442; dilution 1:400; Abcam, Cambridge, MA, USA). This procedure was conducted at MorphoTechnology Corporation in Sapporo, Hokkaido, Japan, following standard protocols. Evaluation of SAβGal activity was performed using X-Gal (Sigma-Aldrich) and a commercial kit (Cellular Senescence Detection Kit Spider BGAL, Dojindo, Osaka, Japan). Olympus BX50 microscope with an OlympusDP70 digital camera (Olympus Corporation, Tokyo, Japan) was used for data collection. WinROOF2018 software (Mitani Corporation, Tokyo, Japan) was used for data collection, and the public domain NIH ImageJ1.54 m program was used for image analysis.

Biochemical analysis

The concentrations of interleukin-1β (IL-1β), transforming growth factor-β1 (TGFβ1) (R&D Systems, Minneapolis, MN), tumor necrosis factor-α (TNFα), monocyte chemoattractant protein-1 (MCP-1) (BD Bioscience, BD OptEIA kits, San Diego, CA), connective tissue growth factor (CTGF) (Abcepta, San Diego, CA), thrombin-antithrombin (TAT; Affinity Biologicals, Ontario, Canada), and D-dimer (Bioss Antibodies, Woburn, MA) were quantified using commercially available enzyme-

linked immunoassays (ELISAs) following the manufacturer's instructions. Collagen type I levels were determined using an ELISA that employed an anti-collagen type I antibody and a biotin-conjugated anti-collagen type I antibody from Rockland Immunochemicals Inc. (Limerick, PA). Creatinine levels were measured using an enzymatic method, while blood urea nitrogen was assessed via a colorimetric method (NCal™ NIST-Calibrated Kit; Arbor Assays, Ann Arbor, MI) following the manufacturer's instructions. Liver-type fatty acid-binding protein (L-FABP) and kidney injury molecule 1 (KIM-1) were quantified using commercial enzyme immunoassay kits (R&D Systems). Corisin levels were measured using an in-house ELISA as previously described[29]. Briefly, a polyclonal anti-transglycosylase 351 antibody was used to coat a 96-well plate at 2 μg/ml in phosphate-buffered saline and incubated overnight at 4 °C. Following blocking with 1% bovine serum albumin in phosphate-buffered saline and thorough washing with phosphate-buffered saline containing Tween, the wells were incubated with varying concentrations of corisin standards and plasma samples at 4 °C overnight. Subsequent washing steps were followed by the addition of horseradish peroxidase-conjugated streptavidin (R&D Systems). After further washing and incubation, a substrate solution was applied for color development, and absorbance was measured at 450 nm using a BIOD-RAD iMark™ microplate reader. Corisin concentrations were calculated from a standard curve, with both inter- and intra-assay variability maintained below 10%.

Determination of albumin-bound corisin and free corisin in serum from DM patients

To assess the presence of free corisin in the serum of patients with diabetes mellitus (DM), 100 μL of tenfold diluted serum was applied to a Nanosep 10 K Omega ultrafiltration device (Pall Corporation, Port Washington, NY, USA). The sample was then centrifuged according to the manufacturer's instructions to separate the serum into two fractions: a flow-through fraction (<10 kDa) and a retained fraction (>10 kDa). Corisin levels were subsequently quantified using enzyme-linked immunosorbent assay (ELISA), as described above, in the >10 kDa retained fraction, <10 kDa flowthrough fraction, and unfractionated serum, the latter representing the total corisin concentration prior to filtration.

Amplification of DNA fragments encoding corisin/corisin-like peptides in healthy subjects and diabetic CKD patients

A large alignment of the polypeptide sequences of the IsaA-like transglycosylases from diverse bacteria was created to develop PCR primers that specifically amplify the DNA encoding the proapoptotic peptides in each urine sample. Two sequences flanking the proapoptotic peptides (SVKAQF and WGTGSV) are highly conserved, and the conserved codon usage in the genes allowed the design of two primers, Corisin-F 5'ATCAGTTAAAGCTCAATTC and Corisin-R 5'GCTACTGAACCAGTACCCCATG, as the forward and reverse primers, respectively. The primer pair amplifies ~150 bp DNA fragments containing the coding sequences of the proapoptotic peptides. The primers were validated by extracting community genomic DNA from the urine of healthy controls ($n = 4$) and patients with diabetic CKD ($n = 18$). The right size fragment was amplified from all extracted genomic DNA, except for the negative control (same PCR mixture, without DNA), and the corisin/corisin-like peptides in the urine samples were obtained by using the DNA sequencing and bioinformatics analyses described below.

Shotgun DNA library construction and sequencing

In this process, each PCR product was resolved in agarose gel and purified (QIAquick PCR purification kit, Qiagen). Importantly, each PCR product was considered a library of the kidneys and urinary tract of a particular CKD patient or healthy control. The DNA was next used in preparing unique libraries by using the NEBNext DNA Library Prep Master Mix Set for Illumina with Unique Dual Indexes to prevent index switching. Library preparations was done using an EpMotion 5075 liquid handler (Eppendorf). The individually barcoded libraries were amplified, quantitated with Qubit and resolved on a Fragment Analyzer to confirm the absence of free primers and primer dimers and the presence of DNA of the expected size. Libraries were pooled in equimolar concentration and further quantitated by qPCR on a BioRad CFX Connect Real-Time System (Bio-Rad Lab Inc., CA). The pooled barcoded shotgun libraries were loaded on a MiSeq flowcell for sequencing (Illumina).

Bioinformatic analyses

Sequences were processed using the TADA Nextflow-based workflow[119,120], which implements protocols for denoising and retaining single-nucleotide resolution amplicon sequence variants (ASVs)[121] from known and custom amplicon sequences. Resulting ASVs were tabulated and quantified per sample, assessed for potential chimeric sequences, and finally compared with known reference sequences using BLASTN[122]. Multiple sequence alignment was performed using DECIPHER[123], with final protein translations performed in R using the Bioconductor Biostrings library[124].

Gene expression analysis

RNA was isolated from kidney cells or tissue using the Sepasol RNA-I Super G reagent from Nacalai Tesque Inc., Kyoto, Japan. Complementary DNA (cDNA) was synthesized from 2 μg of total RNA with an oligo-dT primer and ReverTra Ace Reverse Transcriptase (Toyobo Life Science Department, Osaka, Japan). Standard PCR was then conducted using primers listed in Supplementary Table 3. Depending on the target gene, PCR was performed for 26 to 35 cycles, with denaturation at 94 °C for 30 s, annealing at 65 °C for 30 s, and elongation at 72 °C for 1 min, followed by a final extension at 72 °C for 5 min. mRNA expression levels were normalized to glyceraldehyde 3-phosphate dehydrogenase (GAPDH) mRNA expression.

Single-cell RNA sequencing analysis

Cell culture and processing. Human Renal Proximal Tubule Epithelial Cells (RPTEC) were obtained from LONZA (Houston, TX) and cultured in Renal Epithelial Cell Growth Medium (LONZA) under standard conditions (37 °C, 5% CO_2). At 70% confluency, the culture medium was replaced with fresh medium containing either 20 μg/mL corisin (prepared as a stock solution at 2 mg/mL in 0.5% recombinant human albumin) or 20 μg/mL scrambled peptide in 0.5% recombinant human albumin. Cells were incubated under these conditions for 24 h. After treatment, cells were harvested using trypsinization, washed in cold PBS, pelleted by centrifugation (300 g, 5 min, 4 °C), and cryopreserved in freezing media containing BAMBANKER (GC LYMPHOTEC Inc., Tokyo, Japan). Frozen cells were stored in liquid nitrogen until further processing. Single-cell RNA sequencing was conducted by Takara Bio Inc. (Shiga, Japan) (https://www.takarabio.com/). Cell viability was assessed prior to library preparation using a Countess II Automated Cell Counter (Thermo Fisher Scientific), ensuring >80% viability. Approximately 10,000 cells per sample were loaded into the Chromium Controller (10x Genomics) for droplet encapsulation. The cDNA library was prepared using the Chromium Next GEM Single Cell Fixed RNA Sample Preparation Kit, Chromium Next GEM Chip Q Single Cell Kit, and Dual Index Kit TS Set A (10x Genomics) following the manufacturer's protocols. Sequencing was performed using the Novaseq X Plus system (Illumina) to achieve a target sequencing depth of 50,000–100,000 reads per cell.

Data preprocessing and quality control. Raw sequencing data were demultiplexed, aligned, and quantified into UMI-filtered counts using Cell Ranger (v.4.0.0; 10x Genomics) against the hg38 reference

genome (refdata-gcs-GRCh38-2020-A). Quality control was performed to exclude low-quality cells and artifacts: cells with fewer than 200 detected genes, fewer than 500 UMIs, or greater than 10% mitochondrial gene expression were excluded. After filtering, 9327 cells from corisin-treated samples and 8,186 cells from scrambled peptide-treated samples were retained for downstream analysis.

Data normalization, clustering, and visualization. Normalized gene expression data were generated using the LogNormalize method in the Seurat R package (v.4.0.0), scaling each gene's expression by total UMI counts and multiplying by a scale factor of 10,000. Data were further scaled using the ScaleData function, and highly variable genes were identified for dimensionality reduction. Clustering was performed using the Louvain algorithm implemented in the FindClusters function with a resolution parameter set to 0.3. Uniform Manifold Approximation and Projection (UMAP) was used for dimensionality reduction and visualization with the Seurat RunUMAP function using default parameters.

Trajectory and Differential Gene Expression Analysis. Trajectory analysis was performed using Monocle2 (v.2.20.0), with input gene expression matrices processed through size factor and dispersion estimation steps. Cells were ordered along pseudotime based on the most variable genes, as determined by the "dpFeature" method in Monocle2. Differentially expressed genes (DEGs) were identified using the Seurat FindMarkers function with a Wilcoxon rank-sum test. DEGs were defined by a fold change >2 and P-value < 0.05.

Pathway and Network Analysis. Pathway enrichment analysis was conducted using Enrichr (https://maayanlab.cloud/Enrichr/) with the KEGG and Reactome libraries. Pathways with false discovery rates (FDR) <0.05 were considered significant. Highly upregulated genes in corisin-treated cells were analyzed for protein-protein interactions (PPI) using the STRING database (v.11.5; https://string-db.org/) with a minimum interaction confidence score of 0.7. The resulting PPI networks were visualized and analyzed using Cytoscape (v.3.9.1).

Statistical analysis

Data with a normal distribution are presented as mean ± standard deviation (SD) or standard error of the mean (SEM), while skewed data are expressed as median (interquartile range). Data distribution was assessed using the Shapiro-Wilk or Kolmogorov-Smirnov test. Statistical differences between two normally distributed variables were evaluated using a two-sided unpaired Student's t-test, whereas differences among three or more normally distributed variables were analyzed using one-way analysis of variance (ANOVA) followed by the Newman-Keuls post hoc test. For skewed data, the two-sided Mann-Whitney U test was applied for comparisons between two groups, while the Kruskal-Wallis ANOVA followed by Dunn's post hoc test was used for multiple-group comparisons. The associations between eGFR and other variables were evaluated using univariate and multivariate linear regression analyses. Variables with $p < 0.05$ in the univariate analysis were included in the multivariate model. The non-parametric Spearman's rank correlation coefficient was used to assess correlations between corisin and other variables. Corrections for multiple comparisons were applied where appropriate. A P-value of less than 0.05 was considered statistically significant. Statistical analyses were conducted using GraphPad Prism version 10.5 (GraphPad Software, Inc., San Diego, CA).

Reporting summary

Further information on research design is available in the Nature Portfolio Reporting Summary linked to this article.

Data availability

All data supporting the findings of this study are available within the manuscript, its supplementary materials, and the open-access repository Figshare (https://doi.org/10.6084/m9.figshare.28093115)[125]. The complete sequences of bacterial DNA isolated from the urine of diabetic CKD patients and healthy subjects are available at the at the NCBI BioProject database (https://www.ncbi.nlm.nih.gov/bioproject/PRJNA1218794). Peptides identified from gel bands analyzed by mass spectrometry are accessible via the jPOST repository (https://repository.jpostdb.org/preview/35100932367acebbde2ae2) using the access code 7601. Source data are provided. Source data are provided with this paper.

Code availability

No custom code was developed for this study. All relevant analysis procedures are described in the Methods section.

References

1. Ahmad, E., Lim, S., Lamptey, R., Webb, D. R. & Davies, M. J. Type 2 diabetes. *Lancet* **400**, 1803–1820 (2022).
2. Khan, M. A. B., Hashim, M. J., King, J. K., Govender, R. D., Mustafa, H. & Al Kaabi, J. epidemiology of type 2 diabetes - global burden of disease and forecasted trends. *J. Epidemiol. Glob. Health* **10**, 107–111 (2020).
3. World Health Organization. Diabetes. https://www.who.int/news-room/fact-sheets/detail/diabetes (2021).
4. Sun, H. et al. IDF diabetes atlas: Global, regional and country-level diabetes prevalence estimates for 2021 and projections for 2045. *Diabetes Res Clin. Pr.* **183**, 109119 (2022).
5. Group, T. S. et al. Long-term complications in youth-onset type 2 diabetes. *N. Engl. J. Med* **385**, 416–426 (2021).
6. Harding, J. L., Pavkov, M. E., Magliano, D. J., Shaw, J. E. & Gregg, E. W. Global trends in diabetes complications: a review of current evidence. *Diabetologia* **62**, 3–16 (2019).
7. Shi, Y. & Vanhoutte, P. M. Macro- and microvascular endothelial dysfunction in diabetes. *J. Diabetes* **9**, 434–449 (2017).
8. Strain, W. D. & Paldanius, P. M. Diabetes, cardiovascular disease and the microcirculation. *Cardiovasc Diabetol.* **17**, 57 (2018).
9. Tuttle, K. R. et al. Incidence of Chronic Kidney Disease among Adults with Diabetes, 2015-2020. *N. Engl. J. Med* **387**, 1430–1431 (2022).
10. Widyaputri, F., Rogers, S. L., Kandasamy, R., Shub, A., Symons, R. C. A. & Lim, L. L. Global estimates of diabetic retinopathy prevalence and progression in pregnant women with preexisting diabetes: a systematic review and meta-analysis. *JAMA Ophthalmol.* **140**, 486–494 (2022).
11. Collaboration GBDCKD. Global, regional, and national burden of chronic kidney disease, 1990-2017: a systematic analysis for the Global Burden of Disease Study 2017. *Lancet* **395**, 709–733 (2020).
12. Jadawji, C. et al. Prevalence and progression of diabetic nephropathy in South Asian, white European and African Caribbean people with type 2 diabetes: A systematic review and meta-analysis. *Diabetes Obes. Metab.* **21**, 658–673 (2019).
13. Barrera-Chimal, J. & Jaisser, F. Pathophysiologic mechanisms in diabetic kidney disease: A focus on current and future therapeutic targets. *Diabetes Obes. Metab.* **22**, 16–31 (2020).
14. Samsu, N. Diabetic Nephropathy: Challenges in Pathogenesis, Diagnosis, and Treatment. *Biomed. Res Int* **2021**, 1497449 (2021).
15. Sharma, D., Bhattacharya, P., Kalia, K. & Tiwari, V. Diabetic nephropathy: New insights into established therapeutic paradigms and novel molecular targets. *Diabetes Res Clin. Pr.* **128**, 91–108 (2017).
16. Chung, S., Barnes, J. L. & Astroth, K. S. Gastrointestinal microbiota in patients with chronic kidney disease: a systematic review. *Adv. Nutr.* **10**, 888–901 (2019).

17. Sabatino, A., Regolisti, G., Cosola, C., Gesualdo, L. & Fiaccadori, E. Intestinal microbiota in type 2 diabetes and chronic kidney disease. *Curr. Diab Rep.* **17**, 16 (2017).
18. Yang, G. et al. Role of the gut microbiota in type 2 diabetes and related diseases. *Metabolism* **117**, 154712 (2021).
19. Hu, Z. B. et al. Dysbiosis of intestinal microbiota mediates tubulointerstitial injury in diabetic nephropathy via the disruption of cholesterol homeostasis. *Theranostics* **10**, 2803–2816 (2020).
20. Kikuchi, K. et al. Gut microbiome-derived phenyl sulfate contributes to albuminuria in diabetic kidney disease. *Nat. Commun.* **10**, 1835 (2019).
21. Wang, X. et al. Aberrant gut microbiota alters host metabolome and impacts renal failure in humans and rodents. *Gut* **69**, 2131–2142 (2020).
22. Wong, J., Piceno, Y. M., DeSantis, T. Z., Pahl, M., Andersen, G. L. & Vaziri, N. D. Expansion of urease- and uricase-containing, indole- and p-cresol-forming and contraction of short-chain fatty acid-producing intestinal microbiota in ESRD. *Am. J. Nephrol.* **39**, 230–237 (2014).
23. Liu, X. Y. et al. Kidney microbiota dysbiosis contributes to the development of hypertension. *Gut Microbes* **14**, 2143220 (2022).
24. Gharaie, S. et al. Microbiome modulation after severe acute kidney injury accelerates functional recovery and decreases kidney fibrosis. *Kidney Int* **104**, 470–491 (2023).
25. Saranya, G. R. & Viswanathan, P. Gut microbiota dysbiosis in AKI to CKD transition. *Biomed. Pharmacother.* **161**, 114447 (2023).
26. Shah, N. & Rabb, H. Intestinal microbiota in experimental acute kidney injury. *Nephron* **147**, 25–30 (2023).
27. D'Alessandro-Gabazza, C. N. et al. A Staphylococcus pro-apoptotic peptide induces acute exacerbation of pulmonary fibrosis. *Nat. Commun.* **11**, 1539 (2020).
28. Saiki, H. et al. A microbiome-derived peptide induces apoptosis of cells from different tissues. *Cells* **10**, https://doi.org/10.3390/cells10112885 (2021).
29. D'Alessandro-Gabazza, C. N. et al. Inhibition of lung microbiota-derived proapoptotic peptides ameliorates acute exacerbation of pulmonary fibrosis. *Nat. Commun.* **13**, 1558 (2022).
30. Tsuruga, T. et al. Role of microbiota-derived corisin in coagulation activation during SARS-CoV-2 infection. *J. Thromb. Haemost.* https://doi.org/10.1016/j.jtha.2024.02.014 (2024).
31. Takeshita, A. et al. Thrombomodulin ameliorates transforming growth factor-beta1-mediated chronic kidney disease via the G-protein coupled receptor 15/Akt signal pathway. *Kidney Int* **98**, 1179–1192 (2020).
32. Kastarinen, M. et al. Risk factors for end-stage renal disease in a community-based population: 26-year follow-up of 25,821 men and women in eastern Finland. *J. Intern Med* **267**, 612–620 (2010).
33. Li, G. et al. The role of macrophages in fibrosis of chronic kidney disease. *Biomed. Pharmacother.* **177**, 117079 (2024).
34. Wang, X., Chen, J., Xu, J., Xie, J., Harris, D. C. H. & Zheng, G. The Role of Macrophages in Kidney Fibrosis. *Front Physiol.* **12**, 705838 (2021).
35. Dmytriv, T. R., Storey, K. B. & Lushchak, V. I. Intestinal barrier permeability: the influence of gut microbiota, nutrition, and exercise. *Front Physiol.* **15**, 1380713 (2024).
36. Kratz, F. Albumin as a drug carrier: Design of prodrugs, drug conjugates and nanoparticles. *J. Control Release* **132**, 171–183 (2008).
37. Carter, D. C. & He, X. M. Structure of human serum albumin. *Science* **249**, 302–303 (1990).
38. Carter, D. C. et al. Three-dimensional structure of human serum albumin. *Science* **244**, 1195–1198 (1989).
39. Szekeres, G. P. & Kneipp, J. Different binding sites of serum albumins in the protein corona of gold nanoparticles. *Analyst* **143**, 6061–6068 (2018).
40. Evans, R. et al. Protein complex prediction with AlphaFold-Multimer. *Preprint at bioRxiv* https://doi.org/10.1101/2021.10.04.463034 (2022).
41. Eastman, P. et al. OpenMM 7: Rapid development of high performance algorithms for molecular dynamics. *PLoS Comput Biol.* **13**, e1005659 (2017).
42. Roe, D. R. & Cheatham, T. E. 3rd. PTRAJ and CPPTRAJ: Software for processing and analysis of molecular dynamics trajectory data. *J. Chem. Theory Comput* **9**, 3084–3095 (2013).
43. Bohrmann, B. et al. Endogenous proteins controlling amyloid beta-peptide polymerization. Possible implications for beta-amyloid formation in the central nervous system and in peripheral tissues. *J. Biol. Chem.* **274**, 15990–15995 (1999).
44. Joshi, M. R., Yao, N., Myers, K. A. & Li, Z. Human serum albumin and p53-activating peptide fusion protein is able to promote apoptosis and deliver fatty acid-modified molecules. *PLoS One* **8**, e80926 (2013).
45. Naeem, M., Malik, M.I., Umar, T., Ashraf, S. & Ahmad, A. A Comprehensive Review About Bioactive Peptides: Sources to Future Perspective. *Int. J. Pept. Res. Ther.* **28**, https://doi.org/10.1007/s10989-022-10465-3 (2022).
46. Teow, S. Y. & Ali, S. A. Report: Antibacterial activity of a peptide derived from HIV-1 MN strain gp41 envelope glycoprotein against methicillin-resistant Staphylococcus aureus. *Pak. J. Pharm. Sci.* **29**, 2119–2124 (2016).
47. Wang, C. G., Cheng, F., Xu, L. & Jia, L. Y. HSA targets multiple Aβ42 species and inhibits the seeding-mediated aggregation and cytotoxicity of Aβ42 aggregates. *Rsc Adv.* **6**, 71165–71175 (2016).
48. Xie, H. & Guo, C. Albumin alters the conformational ensemble of amyloid-beta by promiscuous interactions: implications for amyloid inhibition. *Front Mol. Biosci.* **7**, 629520 (2020).
49. Wiggins, R. C., Kshrisagar, B., Kelsch, R. C. & Wilson, B. S. Fragmentation and polymeric complexes of albumin in human urine. *Clin. Chim. Acta* **149**, 155–163 (1985).
50. Yagame, M. et al. Urinary albumin fragments as a new clinical parameter for the early detection of diabetic nephropathy. *Intern Med* **34**, 463–468 (1995).
51. Erkan, E., De Leon, M. & Devarajan, P. Albumin overload induces apoptosis in LLC-PK(1) cells. *Am. J. Physiol. Ren. Physiol.* **280**, F1107–1114 (2001).
52. Ohse, T. et al. Albumin induces endoplasmic reticulum stress and apoptosis in renal proximal tubular cells. *Kidney Int* **70**, 1447–1455 (2006).
53. Zhuang, Y. et al. NLRP3 inflammasome mediates albumin-induced renal tubular injury through impaired mitochondrial function. *J. Biol. Chem.* **289**, 25101–25111 (2014).
54. Fridman D'Alessandro, V. et al. Inhibition of a microbiota-derived peptide ameliorates established acute lung injury. *Am. J. Pathol.* **193**, 740–754 (2023).
55. Sanz, A. B., Sanchez-Nino, M. D., Ramos, A. M. & Ortiz, A. Regulated cell death pathways in kidney disease. *Nat. Rev. Nephrol.* **19**, 281–299 (2023).
56. Zhao, X. C., Livingston, M. J., Liang, X. L. & Dong, Z. Cell apoptosis and autophagy in renal fibrosis. *Adv. Exp. Med Biol.* **1165**, 557–584 (2019).
57. Bao, Y. N. et al. Targeting tumor suppressor p53 for organ fibrosis therapy. *Cell Death Dis.* **15**, 336 (2024).
58. Yan, J., Wang, J., He, J. C. & Zhong, Y. Sirtuin 1 in chronic kidney disease and therapeutic potential of targeting sirtuin 1. *Front Endocrinol. (Lausanne)* **13**, 917773 (2022).
59. Gurkar, A. U. et al. Spatial mapping of cellular senescence: emerging challenges and opportunities. *Nat. Aging* **3**, 776–790 (2023).
60. Pawlikowski, J. S., Adams, P. D. & Nelson, D. M. Senescence at a glance. *J. Cell Sci.* **126**, 4061–4067 (2013).

61. Heckenbach, I. et al. Nuclear morphology is a deep learning biomarker of cellular senescence. *Nat. Aging* **2**, 742–755 (2022).
62. Al-Dabet, M. M. et al. Reversal of the renal hyperglycemic memory in diabetic kidney disease by targeting sustained tubular p21 expression. *Nat. Commun.* **13**, 5062 (2022).
63. Ohtani, N. The roles and mechanisms of senescence-associated secretory phenotype (SASP): can it be controlled by senolysis?. *Inflamm. Regen.* **42**, 11 (2022).
64. Smit, M. A. & Peeper, D. S. Epithelial-mesenchymal transition and senescence: two cancer-related processes are crossing paths. *Aging (Albany NY)* **2**, 735–741 (2010).
65. Wang, M. et al. SIRT1 upregulation promotes epithelial-mesenchymal transition by inducing senescence escape in endometriosis. *Sci. Rep.* **12**, 12302 (2022).
66. Lau, W. L., Chang, Y. & Vaziri, N. D. The consequences of altered microbiota in immune-related chronic kidney disease. *Nephrol. Dial. Transpl.* **36**, 1791–1798 (2021).
67. Lu, C. C. et al. Gut microbiota dysbiosis-induced activation of the intrarenal renin-angiotensin system is involved in kidney injuries in rat diabetic nephropathy. *Acta Pharm. Sin.* **41**, 1111–1118 (2020).
68. Fang, Q. et al. Roles of gut microbial metabolites in diabetic kidney disease. *Front Endocrinol. (Lausanne)* **12**, 636175 (2021).
69. Kanbay, M. et al. The crosstalk of gut microbiota and chronic kidney disease: role of inflammation, proteinuria, hypertension, and diabetes mellitus. *Int Urol. Nephrol.* **50**, 1453–1466 (2018).
70. Cai, K. et al. Changes of gut microbiota in diabetic nephropathy and its effect on the progression of kidney injury. *Endocrine* **76**, 294–303 (2022).
71. Nishiwaki, R. et al. Elevated plasma and bile levels of corisin, a microbiota-derived proapoptotic peptide, in patients with severe acute cholangitis. *Gut Pathog.* **15**, 59 (2023).
72. Zhang, J. Q. et al. Cellular senescence of renal tubular epithelial cells in renal fibrosis. *Front Endocrinol. (Lausanne)* **14**, 1085605 (2023).
73. Antar, S.A., Ashour, N.A., Marawan, M.E. & Al-Karmalawy, A.A. Fibrosis: Types, effects, markers, mechanisms for disease progression, and its relation with oxidative stress, immunity, and inflammation. *Int J Mol Sci* **24**, https://doi.org/10.3390/ijms24044004 (2023).
74. Panizo, S. et al. Fibrosis in chronic kidney disease: pathogenesis and consequences. *Int J Mol Sci* **22**, https://doi.org/10.3390/ijms22010408 (2021).
75. Wynn, T. A. Cellular and molecular mechanisms of fibrosis. *J. Pathol.* **214**, 199–210 (2008).
76. Zeisberg, M. & Kalluri, R. Cellular mechanisms of tissue fibrosis. 1. Common and organ-specific mechanisms associated with tissue fibrosis. *Am. J. Physiol. Cell Physiol.* **304**, C216–225 (2013).
77. Amorim, R. G., Guedes, G. D., Vasconcelos, S. M. D. & Santos, J. C. D. Kidney disease in diabetes mellitus: cross-linking between hyperglycemia, redox imbalance and inflammation. *Arq. Bras. Cardiol.* **112**, 577–586 (2019).
78. Kriz, W., Kaissling, B. & Le Hir, M. Epithelial-mesenchymal transition (EMT) in kidney fibrosis: fact or fantasy?. *J. Clin. Invest* **121**, 468–474 (2011).
79. Lovisa, S., Zeisberg, M. & Kalluri, R. Partial epithelial-to-mesenchymal transition and other new mechanisms of kidney fibrosis. *Trends Endocrinol. Metab.* **27**, 681–695 (2016).
80. Sheng, L. & Zhuang, S. New insights into the role and mechanism of partial epithelial-mesenchymal transition in kidney fibrosis. *Front Physiol.* **11**, 569322 (2020).
81. Childs, B. G., Baker, D. J., Kirkland, J. L., Campisi, J. & van Deursen, J. M. Senescence and apoptosis: dueling or complementary cell fates?. *EMBO Rep.* **15**, 1139–1153 (2014).
82. Cohn, R. L., Gasek, N. S., Kuchel, G. A. & Xu, M. The heterogeneity of cellular senescence: insights at the single-cell level. *Trends Cell Biol.* **33**, 9–17 (2023).
83. Childs, B. G. et al. Senescent cells: an emerging target for diseases of ageing. *Nat. Rev. Drug Discov.* **16**, 718–735 (2017).
84. Sasaki, M., Kumazaki, T., Takano, H., Nishiyama, M. & Mitsui, Y. Senescent cells are resistant to death despite low Bcl-2 level. *Mech. Ageing Dev.* **122**, 1695–1706 (2001).
85. Hoffmann, J. et al. Aging enhances the sensitivity of endothelial cells toward apoptotic stimuli: important role of nitric oxide. *Circ. Res* **89**, 709–715 (2001).
86. Hampel, B., Malisan, F., Niederegger, H., Testi, R. & Jansen-Durr, P. Differential regulation of apoptotic cell death in senescent human cells. *Exp. Gerontol.* **39**, 1713–1721 (2004).
87. Zhang, J., Patel, J. M. & Block, E. R. Enhanced apoptosis in prolonged cultures of senescent porcine pulmonary artery endothelial cells. *Mech. Ageing Dev.* **123**, 613–625 (2002).
88. Fanali, G., di Masi, A., Trezza, V., Marino, M., Fasano, M. & Ascenzi, P. Human serum albumin: from bench to bedside. *Mol. Asp. Med* **33**, 209–290 (2012).
89. Yamasaki, K., Chuang, V. T., Maruyama, T. & Otagiri, M. Albumin-drug interaction and its clinical implication. *Biochim Biophys. Acta* **1830**, 5435–5443 (2013).
90. Belinskaia, D.A., Voronina, P.A., Shmurak, V.I., Jenkins, R.O. & Goncharov, N.V. Serum albumin in health and disease: esterase, antioxidant, transporting and signaling properties. *Int. J. Mol. Sci.* **22**, https://doi.org/10.3390/ijms221910318 (2021).
91. Nielsen, R., Christensen, E. I. & Birn, H. Megalin and cubilin in proximal tubule protein reabsorption: from experimental models to human disease. *Kidney Int* **89**, 58–67 (2016).
92. Grams, M. E., Astor, B. C., Bash, L. D., Matsushita, K., Wang, Y. & Coresh, J. Albuminuria and estimated glomerular filtration rate independently associate with acute kidney injury. *J. Am. Soc. Nephrol.* **21**, 1757–1764 (2010).
93. Matsushita, K. et al. Estimated glomerular filtration rate and albuminuria for prediction of cardiovascular outcomes: a collaborative meta-analysis of individual participant data. *Lancet Diabetes Endocrinol.* **3**, 514–525 (2015).
94. Writing Group for the CKDPC,et al. Estimated glomerular filtration rate, albuminuria, and adverse outcomes: An individual-participant data meta-analysis. *JAMA* **330**, 1266-1277 (2023).
95. Amsellem, S. et al. Cubilin is essential for albumin reabsorption in the renal proximal tubule. *J. Am. Soc. Nephrol.* **21**, 1859–1867 (2010).
96. Birn, H. et al. Cubilin is an albumin binding protein important for renal tubular albumin reabsorption. *J. Clin. Invest* **105**, 1353–1361 (2000).
97. Boger, C. A. et al. CUBN is a gene locus for albuminuria. *J. Am. Soc. Nephrol.* **22**, 555–570 (2011).
98. American diabetes association professional practice c. 2. classification and diagnosis of diabetes: Standards of medical care in diabetes-2022. *Diabetes Care* **45**, S17-S38 (2022).
99. Kidney disease: improving global outcomes CKDWG. KDIGO 2024 clinical practice guideline for the evaluation and management of chronic kidney disease. *Kidney Int.* **105**, S117-S314 (2024).
100. Levin, A. et al. Executive summary of the KDIGO 2024 clinical practice guideline for the evaluation and management of chronic kidney disease: known knowns and known unknowns. *Kidney Int* **105**, 684–701 (2024).
101. Martinez, L., Andrade, R., Birgin, E. G. & Martinez, J. M. PACKMOL: a package for building initial configurations for molecular dynamics simulations. *J. Comput Chem.* **30**, 2157–2164 (2009).
102. Braun, E. et al. Best practices for foundations in molecular simulations [Article v1.0]. *Living J. Comput. Mol. Sci.* **1**, https://doi.org/10.33011/livecoms.1.1.5957 (2019).
103. Ryckaert, J.-P., Ciccotti & GB, H. J. C. Numerical integration of the cartesian equations of motion of a system with constraints: molecular dynamics of n-alkanes. *J. Comput Phys.* **23**, 327–341 (1977).

104. Hopkins, C. W., Le Grand, S., Walker, R. C. & Roitberg, A. E. Long-time-step molecular dynamics through hydrogen mass repartitioning. *J. Chem. Theory Comput* **11**, 1864–1874 (2015).
105. Bowman, G. R., Ensign, D. L. & Pande, V. S. Enhanced modeling via network theory: adaptive sampling of markov state models. *J. Chem. Theory Comput* **6**, 787–794 (2010).
106. Husic, B. E. & Pande, V. S. Markov state models: from an art to a science. *J. Am. Chem. Soc.* **140**, 2386–2396 (2018).
107. Lane, T. J., Shukla, D., Beauchamp, K. A. & Pande, V. S. To milliseconds and beyond: challenges in the simulation of protein folding. *Curr. Opin. Struct. Biol.* **23**, 58–65 (2013).
108. Shukla, D., Hernandez, C. X., Weber, J. K. & Pande, V. S. Markov state models provide insights into dynamic modulation of protein function. *Acc. Chem. Res* **48**, 414–422 (2015).
109. Scherer, M. K. et al. PyEMMA 2: A software package for estimation, validation, and analysis of markov models. *J. Chem. Theory Comput* **11**, 5525–5542 (2015).
110. Wu, H. & Noé, F. Variational approach for learning markov processes from time series data. *J. Nonlinear Sci.* **30**, 23–66 (2020).
111. Prinz, J. H. et al. Markov models of molecular kinetics: generation and validation. *J. Chem. Phys.* **134**, 174105 (2011).
112. Noe, F., Schutte, C., Vanden-Eijnden, E., Reich, L. & Weikl, T. R. Constructing the equilibrium ensemble of folding pathways from short off-equilibrium simulations. *Proc. Natl Acad. Sci. USA* **106**, 19011–19016 (2009).
113. McGibbon, R. T. et al. MDTraj: A modern open library for the analysis of molecular dynamics trajectories. *Biophys. J.* **109**, 1528–1532 (2015).
114. Humphrey, W., Dalke, A. & Schulten, K. VMD: visual molecular dynamics. *J. Mol. Graph* **14**, 27–38 (1996).
115. Hunter, J. D. Matplotlib: A 2D Graphics Environment. *J. Environ. Public Health* **9**, 90–95 (2007).
116. Best, R. B., Hummer, G. & Eaton, W. A. Native contacts determine protein folding mechanisms in atomistic simulations. *Proc. Natl Acad. Sci. USA* **110**, 17874–17879 (2013).
117. Case, D. A. et al. The Amber biomolecular simulation programs. *J. Comput Chem.* **26**, 1668–1688 (2005).
118. Aqvist, J., Luzhkov, V. B. & Brandsdal, B. O. Ligand binding affinities from MD simulations. *Acc. Chem. Res* **35**, 358–365 (2002).
119. Di Tommaso, P., Chatzou, M., Floden, E. W., Barja, P. P., Palumbo, E. & Notredame, C. Nextflow enables reproducible computational workflows. *Nat. Biotechnol.* **35**, 316–319 (2017).
120. Ras, V. et al. Using a multiple-delivery-mode training approach to develop local capacity and infrastructure for advanced bioinformatics in Africa. *PLoS Comput Biol.* **17**, e1008640 (2021).
121. Callahan, B. J., McMurdie, P. J., Rosen, M. J., Han, A. W., Johnson, A. J. & Holmes, S. P. DADA2: High-resolution sample inference from Illumina amplicon data. *Nat. Methods* **13**, 581–583 (2016).
122. Altschul, S. F., Gish, W., Miller, W., Myers, E. W. & Lipman, D. J. Basic local alignment search tool. *J. Mol. Biol.* **215**, 403–410 (1990).
123. Wright, E. S. DECIPHER: harnessing local sequence context to improve protein multiple sequence alignment. *BMC Bioinforma.* **16**, 322 (2015).
124. Gentleman, R. C. et al. Bioconductor: open software development for computational biology and bioinformatics. *Genome Biol.* **5**, R80 (2004).
125. Yasuma, T. et al. Microbiota-derived corisin accelerates kidney fibrosis by promoting cellular aging. figshare. Dataset. https://doi.org/10.6084/m9.figshare.28093115 (2025).

Acknowledgements

This study was financially supported in part by grants from the Japan Science and Technology Agency (JST) (Grant No JPMJFR2216; T.Y.) the Japan Society for the Promotion of Science (Grant No. 22K08280; C.N.D-G.) the 2022 Takeda Science Foundation (T.Y.), the 2023 Takeda Science Foundation (E.C.G.) a grant from the Japan Association for Diabetes Education and Care (T.Y.) the Eli Lilly Japan Innovation Research Grant 2023 (T.Y.) and Daiwa Security Foundation 2024 (T.Y.) and in part by a gift from the Charles and Margaret Levin Family Foundation to IC and ECG. The funders had no role in study design, data analysis, decision to publish, or manuscript preparation.

Author contributions

T.Y., C.N.D-G., H.F.: preparation of disease models, preparation of the first manuscript draft. M.T., M.U., A.Ta., K.N., Y.Y., T.A.: analysis of gene and protein expression. I.C., J.A., A.M.A-H., M.A.B.A.: preparation of proteins, genome analysis, chromatography. T.K., H.F., T.O., Y.O., A.To., C.I.: clinical evaluation of subjects, provision of clinical data and samples. M.T., V.F.D.: flow cytometry analyses, gene, and protein expression analysis, Western blotting. X.M., D.S.: Molecular dynamics simulations. C.J.F: Determination of corisin and corisin-like sequences in human samples. I.C., E.C.G., O.H., T.K.: study design, analysis, and interpretation of the data, preparation, and correction of the manuscript. T.N., H.Y., R.O., R.I.M., K.L., M.R.K.: intellectual contribution and interpretation of the data.

Competing interests

E.C.G. and Y.Y. have a patent on the TGFβ1 TG mice used in the present study. In addition, there is an invention disclosure by C.N.D.G., E.C.G. and I.C. on the corisin peptide and anticorisin mAtb developed for the treatment of organ fibrosis described in this study. The remaining authors declare no competing interests.

Additional information

Supplementary information The online version contains supplementary material available at https://doi.org/10.1038/s41467-025-61847-2.

Correspondence and requests for materials should be addressed to Tetsu Kobayashi, Isaac Cann or Esteban C. Gabazza.

Peer review information *Nature Communications* thanks the anonymous reviewers for their contribution to the peer review of this work. A peer review file is available.

[1]Department of Immunology, Mie University Faculty and Graduate School of Medicine, Edobashi 2-174, Tsu, Mie, Japan. [2]Microbiome Research Center, Mie University, Edobashi 2-174, Tsu, Mie, Japan. [3]Department of Diabetes, Metabolism and Endocrinology, Mie University Faculty and Graduate School of Medicine, Edobashi 2-174, Tsu, Mie, Japan. [4]Department of Pulmonary and Critical Care Medicine, Mie University Faculty and Graduate School of Medicine, Edobashi 2-174, Tsu, Mie, Japan. [5]Carl R. Woese Institute for Genomic Biology (Microbiome Metabolic Engineering), University of Illinois Urbana-Champaign, Urbana, IL, USA. [6]Division of Nutritional Sciences, University of Illinois Urbana-Champaign, Urbana, IL, USA. [7]Microbial Discovery Group, 7420 S Howell Ave, Oak Creek, WI, USA. [8]Department of Microbiology and Molecular Genetics, Mie University Graduate School of Medicine, Edobashi 2-174, Tsu, Mie, Japan. [9]Department of Stem Cell and Developmental Biology, Mie University Graduate School of Medicine, Edobashi 2-174, Tsu, Mie, Japan. [10]W.M. Keck Center for Functional and Comparative Genomics, University of Illinois Urbana-Champaign, Urbana, IL, USA. [11]Department of Animal Science, University of Illinois Urbana-Champaign, Urbana, IL, USA. [12]Department of Chemical and Biomolecular Engineering, University of Illinois Urbana-Champaign, Urbana, IL, USA. [13]Roy J. Carver Biotechnology Center, University of Illinois Urbana-Champaign, Urbana, IL, USA. [14]Respiratory Center, Matsusaka Municipal Hospital, Tonomachi 1550, Matsusaka, Mie, Japan. [15]The School of Molecular and Cellular Biology, University of Illinois Urbana-Champaign, Urbana, IL, USA. [16]Department of Microbiology, University of Illinois Urbana–Champaign, Urbana, IL, USA. [17]Center for East Asian & Pacific Studies, University of Illinois Urbana–Champaign, Urbana, IL, USA. [18]These authors contributed equally: Taro Yasuma, Hajime Fujimoto, Corina N. D'Alessandro-Gabazza, Masaaki Toda.
✉e-mail: ktetsu@clin.medic.mie-u.ac.jp; icann@illinois.edu; gabazza@med.mie-u.ac.jp